

# Journal Pre-proof

CeO<sub>2</sub>/g-C<sub>3</sub>N<sub>4</sub>/V<sub>2</sub>O<sub>5</sub> ternary nano hetero-structures decorated with CQDs for enhanced photo-reduction capabilities under different light sources: Dual Z-scheme mechanism

Amit Kumar, Sunil Kumar Sharma, Gaurav Sharma, Mu. Naushad, Florian J. Stadler

PII: S0925-8388(20)32056-9

DOI: <https://doi.org/10.1016/j.jallcom.2020.155692>

Reference: JALCOM 155692

To appear in: *Journal of Alloys and Compounds*

Received Date: 13 February 2020

Revised Date: 14 May 2020

Accepted Date: 16 May 2020

Please cite this article as: A. Kumar, S.K. Sharma, G. Sharma, M. Naushad, F.J. Stadler, CeO<sub>2</sub>/g-C<sub>3</sub>N<sub>4</sub>/V<sub>2</sub>O<sub>5</sub> ternary nano hetero-structures decorated with CQDs for enhanced photo-reduction capabilities under different light sources: Dual Z-scheme mechanism, *Journal of Alloys and Compounds* (2020), doi: <https://doi.org/10.1016/j.jallcom.2020.155692>.

This is a PDF file of an article that has undergone enhancements after acceptance, such as the addition of a cover page and metadata, and formatting for readability, but it is not yet the definitive version of record. This version will undergo additional copyediting, typesetting and review before it is published in its final form, but we are providing this version to give early visibility of the article. Please note that, during the production process, errors may be discovered which could affect the content, and all legal disclaimers that apply to the journal pertain.

© 2020 Published by Elsevier B.V.



**Credit authorship contribution statement**

**Amit Kumar:** Conceptualization- original draft, Writing - review & editing. **Sunil Kumar Sharma:** Data curation and experimental. **Gaurav Sharma:** Contribution to original draft, **Mu. Naushad:** Reviewing, Characterization Investigation. **Florian J. Stadler:** Supervision, Reviewing & Editing

Journal Pre-proof

**CeO<sub>2</sub>/g-C<sub>3</sub>N<sub>4</sub>/V<sub>2</sub>O<sub>5</sub> ternary nano hetero-structures decorated with CQDs for enhanced photo-reduction capabilities under different light sources: Dual Z-scheme mechanism**

Amit Kumar<sup>a,b,\*</sup>, Sunil Kumar Sharma<sup>a</sup>, Gaurav Sharma<sup>a,b</sup>, Mu. Naushad<sup>c</sup>, Florian J. Stadler<sup>a,\*\*</sup>

<sup>a</sup>*College of Materials Science and Engineering, Shenzhen Key Laboratory of Polymer Science and Technology, Guangdong Research Center for Interfacial Engineering of Functional Materials, Nanshan District Key Laboratory for Biopolymers and Safety Evaluation, Shenzhen University, Shenzhen, 518055, PR China*

<sup>b</sup>*School of Chemistry, Shoolini University, Solan, Himachal Pradesh, India-173229*

<sup>c</sup>*Department of Chemistry, College of Science, Building#5, King Saud University, Riyadh 11451, Saudi Arabia*

\* [mittuchem83@gmail.com](mailto:mittuchem83@gmail.com), \*\* [fjstadler@szu.edu.cn](mailto:fjstadler@szu.edu.cn)

**Abstract**

In this work, a carbon quantum dots (CQDs) decorated dual Z-scheme CeO<sub>2</sub>/g-C<sub>3</sub>N<sub>4</sub>/V<sub>2</sub>O<sub>5</sub> heterojunction (CCGV) was rationally synthesized by simple hydrothermal method. The crystal structure, morphology, and optical properties of the photocatalysts were characterized by X-ray diffraction (XRD), scanning electron microscopy (SEM), transmission electron microscopy (TEM), X-ray photoelectron spectroscopy (XPS) and UV-Vis diffuse reflectance spectroscopy. CCGV catalyst shows high visible absorption, including near infra-red region and solar light via two-channel charge transfer (dual Z-scheme), reduced recombination, and up-conversion effect of CQDs. The heterojunction was used for visible assisted photo-reduction of carcinogenic hexavalent chromium ions (Cr(VI)) with a 99% reduction in 100 min without any sacrificial agent or hole scavenger. The reaction becomes more rapid with tartaric acid as a scavenger with a complete reduction in just 30 min under visible light. Photogenerated electrons are the dominant active species, followed by  $\bullet\text{O}_2^-$ , as revealed by the scavenging experiments. The use of sacrificial agents and scavengers suggests that

photogenerated electrons were the dominant active species followed by  $\bullet\text{O}_2^-$  radicals. The electrochemical impedance spectroscopy and photoluminescence results confirm highly reduced recombination, high charge separation, and charge transfer capacity in the dual Z-scheme heterojunction. The conduction band edges of  $\text{CeO}_2$  and  $\text{V}_2\text{O}_5$  (which are protected by the dual charge transfer) have an appropriate potential for the rapid reduction of hexavalent chromium. The XPS scan of the catalyst after separation shows the presence of Cr in the +3 oxidation state, suggesting complete photo-reduction. This study is promising for developing wide spectrum active simple heterojunction photocatalysts for pollutant removal with high efficiency.

**Keywords:**  $\text{CeO}_2$ ; Photocatalysis; Heterojunction; Cr(VI) reduction; carbon nitride; Z-scheme

## 1. Introduction

The rapid industrialization and anthropogenic activities have caused detrimental effects on the ecosystem by severe environmental contamination. With ongoing water quality deterioration, various renewable and greener methods for efficient elimination of emerging toxic pollutants have been explored by researchers and environmentalists [1, 2]. The world health organization (WHO) data shows that 844 million people do not have access to basic drinking water facilities, and these numbers will further increase tremendously in the future [3]. Wastewater often contains numerous organic contaminants and heavy metals, which, when entering drinking water supplies, cause health hazards [4, 5]. The increasing heavy toxic metal contaminations due to industrial and mining discharges have created numerous health issues [6, 7]. Among various heavy metal contaminants, carcinogenic, and mutagenic hexavalent chromium Cr(VI) is responsible for various chronic health disorders [8, 9]. Cr(VI) has high solubility and mobility in water resources and originates from chromium  $\text{Cr}_2\text{O}_7^{2-}$  and  $\text{CrO}_4^{2-}$  ions. Cr(VI) produces reactive oxygen species and damages the organelles of the living cells by penetrating caused by its high solubility [10]. On the other hand, Cr(III) is

nearly 1000 times less toxic than Cr(VI) but has low mobility, and the former can be precipitated as Cr(OH)<sub>3</sub> in neutral or basic media [11]. Thus one of the most successful routes to remove toxic Cr(VI) is the reduction to Cr(III). Here photocatalytic reduction is the most promising choice because the process is easy and efficient. Especially, utilizing solar or visible light energy for photocatalytic water treatment is essential for practical and large scale utilization [12].

However, single-phase semiconductor photocatalysts suffer from severe limitations on their performance, including limited spectrum activity, low quantum yield and high charge carrier recombination. The catalytic degradation performance of photocatalytic materials can be improved by suppressing the charge carrier recombination on the photocatalyst [13]. These limitations have been most effectively addressed by forming heterojunctions using different semiconductors with optimum bandgap and electronic band arrangement for maximum optical absorption and electronic movement [14, 15]. The synergistic performance of the semiconductors involved in a hetero-structure or junction involving two semiconductors is highly beneficial for outstanding photo-oxidation and photo-reduction of pollutants [16, 17]. Z-scheme heterojunctions photocatalysts derive their charge transfer mechanism from natural photosynthesis and accelerate the photogenerated charge carriers separation and transfer [18]. In a Z-scheme transfer pathway, not only recombination is inhibited, but also, the more negative CB and positive VB potential is maintained for effective generation of radicals. The introduction of a third counterpart semiconductor is encouraging, as this further elevates the photocatalytic activity by allowing for charge transfer by a dual Z-scheme mechanism. In a dual Z-scheme transfer mechanism, the first component is having a higher a CB with two e<sup>-</sup> transmission channels [19]. Along with the interface, the photogenerated electrons on component 2 are transferred to the other two components, leading to highly improved

separation. Thus the highly placed conduction bands of two components can generate sufficient superoxide radicals, and more hydroxyl radicals are generated on the valence bands.

Among various semiconductors,  $V_2O_5$  is widely used as a potent environmental catalyst because of its low cost and non-toxic nature.  $V_2O_5$  has a wide range of properties, such as lower bandgap, chemical stability and lack of toxicity. It has been used in various applications such as antifungal and antimicrobial additives to textiles and during the wastewater treatment [20, 21].  $CeO_2$  is a rare earth semiconductor catalyst that has grabbed the attention because of its stability and strong oxidizing capability. Ceria has ample oxygen vacancies and high oxygen storage capacity with the ability to utilize and release oxygen via the  $Ce^{3+}/Ce^{4+}$  redox cycle [22]. Hence,  $CeO_2$  is frequently used in environmental catalysis, water splitting, sensing applications [23-25] and particularly in photocatalysis [26].

As an organic semiconductor, graphitic carbon nitride ( $g-C_3N_4$ ) as a metal-free conjugated polymer has been reported as the most popular photocatalyst for environmental clean-up and energy production [27, 28].  $g-C_3N_4$  is a tough semiconductor that has unique electrical, thermal, and optical properties [29]. It has an energy bandgap of nearly 2.7 eV and shows exceptional thermal and chemical stability because of tri-s-triazine based building blocks [16] and is used as visible-light responsive photocatalyst [30]. On the other hand, various drawbacks, including fast charge recombination and poor visible light absorption, limit its photocatalytic performance. Structural modifications and amino group regulation have been performed to increase the catalytic activity [31]. Various heterojunctions have been formed to improve its photocatalytic activity [32]. Metal oxides as  $Fe_2O_3$  have been incorporated to form  $rGO/Fe_2O_3/g-C_3N_4$  nanostructures with rapid photoexcited charge transfer via nano-channels [33]. Various dual Z-scheme junctions utilizing  $g-C_3N_4$  such as  $MoS_2/g-C_3N_4/Bi_{24}O_{31}Cl_{10}$  [34],  $Ag_3PO_4/AgBr/g-C_3N_4$  [35], and  $AgI/LaFeO_3/g-C_3N_4$  [36] have been prepared with enhanced photocatalytic activity. Compared with various other materials,

quantum dots (QDs) possess highly efficient electron transport capacity, which leads to rapid transfer electrons and holes to the catalyst surface from inside or core. This substantially improves the photocatalytic performance and quantum efficiency [37]. Carbon quantum dots have been used photocatalysis as an active part of Z-scheme junctions as well as of dual Z-scheme based ternary heterojunctions. CQDs have interesting electronic properties and also possess fluorescence emission. Also, they show up-conversion properties and can enhance the visible light absorption by light generated electron transfer [38] and electrons-oxygen interactions. They also participate in the Z-scheme electron transfer in addition to extending the light spectrum absorption. Various Z-scheme and dual Z-scheme mechanism-based junctions have been prepared for photocatalytic reduction of hexavalent Cr, as listed in Table1.

In light of the above, a dual Z-scheme  $V_2O_5/CeO_2/g-C_3N_4$  ternary heterojunction has been prepared, followed by modification with CQDs for better visible and solar photocatalytic activity. The mechanistic route to enhanced photocatalysis has been explained based on a direct dual-Z-scheme charge carrier in comparison to a conventional type-II heterojunction that has been elaborately discussed. This ternary hybrid heterojunction exhibits exceptional charge separation and protection of high potential CBs via dual Z-scheme transfer and bridging action by CQDs. It is still challenging to fabricate semiconductor composites with coherent interfacial contact & suitable band edge placements and improving the photocatalytic potential of  $g-C_3N_4$  via the addition of suitable semiconductors. In addition, CQDs act as bridging material for effective dual Z-scheme transfer. Their electron-accepting property promotes the formation of more reactive oxygen species and augments the lifetime of charge carriers for high performance wide spectral photo-reductive and photo-oxidative applications.

## 2. Experimental

### 2.1 Synthesis of g-C<sub>3</sub>N<sub>4</sub>

The g-C<sub>3</sub>N<sub>4</sub> was prepared by the thermal treatment of urea. 10 g of powdered urea was calcined at 450°C for 3 h in a silica crucible and 10°C min<sup>-1</sup> heating rate. After this, the deammoniation was done at 500°C for 2h. The yellowish g-C<sub>3</sub>N<sub>4</sub> powder was then washed with ethanol and water repeatedly and dried at 80°C.

### 2.2 Synthesis of CeO<sub>2</sub> nanoparticles

The CeO<sub>2</sub> nanoparticles were synthesized by a hydrothermal route. In a typical method, 0.002 moles of Ce(NO<sub>3</sub>)<sub>3</sub> and 0.004 mol of PVP was dispersed in 40 mL double distilled water. The suspension was then transferred to a 50 mL and heated at 200°C for 2.5 h in an autoclave. The prepared CeO<sub>2</sub> nanoparticles were then repeatedly washed with water/ethanol and freeze-dried under vacuum.

### 2.3 Synthesis of CQDs decorated CeO<sub>2</sub>/g-C<sub>3</sub>N<sub>4</sub>/V<sub>2</sub>O<sub>5</sub> dual Z-scheme heterojunction (CCGV)

In another procedure, 2.9 g ammonium metavanadate (NH<sub>4</sub>VO<sub>3</sub>) was added to 100 mL ethylene glycol. The resulting mixture was then heated to 110°C with continuous stirring followed by refluxing at 160°C for 1h. Thus vanadyl glycolate (VEG) is precipitated. To VEG precursor, 0.3 g of g-C<sub>3</sub>N<sub>4</sub> and 0.3 g of CeO<sub>2</sub> nanoparticles were added, followed by sonication for 1h. The resultant mixture was then annealed at 500°C for 2 h. CeO<sub>2</sub>/g-C<sub>3</sub>N<sub>4</sub>/V<sub>2</sub>O<sub>5</sub> catalyst was thus formed. The vacuum dried catalyst was dipped in CQDs (procured from Sigma Aldrich, AR) suspension and autoclaved at 180°C for 24 h. The obtained CQDs@CeO<sub>2</sub>/g-C<sub>3</sub>N<sub>4</sub>/V<sub>2</sub>O<sub>5</sub> catalyst was then washed repeatedly with distilled water and vacuum dried at 80°C. The synthesis scheme is represented in Figure 1.

### 2.4 Characterization

A Rigaku (D/MAX-2500) X-ray diffractometer was employed to determine the crystal structure and phase purity of single and ternary photocatalysts. The surface morphology and

shape of the ternary heterojunction was analyzed by scanning electron microscopy (LEO 435 VP instrument) and microstructure by TEM, ESCA transmission electron microscope. The specific surface area was measured by the Brunauer–Emmett–Teller (BET) method with a NOVA 1200 analyzer. The elemental and oxidation state analysis was done by X-ray photoelectron spectroscopy measurements using a K-alpha XPS (Thermo VG Scientific) instrument with an Al K $\alpha$  X-ray monochromating source.

### 2.5 Optical and electrochemical experiments

The UV-visible diffuse reflectance spectra (UV-DRS) were captured using a Hitachi U-2550 instrument (BaSO<sub>4</sub> standard method). The potential band edges for these photocatalysts were then calculated by using following equation [39]:

$$E_{VB} = X - E^e + 0.5E_g \quad (1)$$

$$E_{CB} = E_{VB} - E_g \quad (2)$$

Where  $E_{CB}$  and  $E_{VB}$  signify band conduction and valence band edges respectively,  $E^e = \sim 4$  eV (electron energy on hydrogen scale),  $X$  is the geometric mean of Pearson absolute electronegativity (PAE), and  $E_g$  denotes the bandgap. The Photoluminescence (PL) spectra of single and ternary heterojunctions were obtained using a Hitachi fluorescence spectrophotometer for determining the extent of recombination of electrons and holes. The electrochemical impedance spectroscopy (EIS) was also performed on synthesized photocatalysts. The experiments were performed on CHI 660D three-electrode system based workstation. The sample modified carbon electrode was employed as a working electrode, Ag/AgCl working electrode, and a Pt wire counter electrode. The impedance measurements were done in Na<sub>2</sub>SO<sub>4</sub> (0.2 mol/L, pH 7) solution as electrolyte (0.2 V; frequency 0.1 Hz - 100 kHz).

### 2.6 Photo-reduction of Cr(VI)

Journal Pre-proof

The photocatalytic potential of g-C<sub>3</sub>N<sub>4</sub>, V<sub>2</sub>O<sub>5</sub>, CeO<sub>2</sub>, and CCGV junction was tested for visible light and sunlight assisted reduction of Cr(VI) into Cr(III). A 300 W xenon lamp with visible (480 mW cm<sup>-2</sup>) and NIR filter (200 mW cm<sup>-2</sup>) was used as the light source in an automated photo-reactor (TOPTION). The temperature inside the reactor was maintained at 30 ± 0.5 °C with the help of water circulation. A distance of 10 cm between the lamp and reaction system was maintained. The batch reduction experiments were performed firstly under Xe lamp (visible), and all the reaction parameters were studied. The operations conditions are as follows: [Catalyst] = 0.3 mg/mL, [Cr (VI)] = 20 mg L<sup>-1</sup> and pH = 2 were fixed. In a typical methodology, 30 mg catalyst was dispersed into a 100 mL Cr<sup>6+</sup> solution with constant stirring. After exposure to the lamp, the fall in Cr(VI) concentration was monitored as a function of time. For each measurement, 3 ml aliquots were extracted from the reaction medium, followed by centrifugation and filtration using a membrane filter (0.45µm Teflon). Diphenylcarbazide colorimetric method was used for estimating residual Cr<sup>6+</sup> concentration by recording the absorbance at 540 nm on Shimadzu 2202 spectrophotometer. The experiments were also carried out under NIR light and natural sunlight.

### 3. Results

#### 3.1 Material characterization

##### 3.1.1 XRD analysis

Figure 2 shows the XRD patterns of as-synthesized CeO<sub>2</sub>, g-C<sub>3</sub>N<sub>4</sub>, V<sub>2</sub>O<sub>5</sub>, and CCGV photocatalysts. The diffractogram for g-C<sub>3</sub>N<sub>4</sub> shows characteristic peaks at 12.8° and 27.4° corresponding to (100) in-plane structural repeating unit and periodic stacking of layers along the (002) planes, respectively (JCPDS 87-1526) [40]. The diffraction pattern for CeO<sub>2</sub> shows peaks for (111), (220), (311), (222), (200), (331) and (400) diffraction planes for face-centered cubic structure in agreement with standard JCPDS card No. 34-0394 [41]. For V<sub>2</sub>O<sub>5</sub>

the characteristic peaks for (020), (001), (110), (040), (101), (012), (102), (200), (200), (201) and (170) planes of the orthorhombic phase of  $V_2O_5$ , which is in good agreement with JCPDS card no. 89-2482 [42]. The XRD pattern for the junction shows all the peaks for  $CeO_2$ ,  $g-C_3N_4$ , and  $V_2O_5$  are observed with the same phases. Therefore, the nature of all the three components is preserved during synthesis, although as compared to the bare semiconductors, slight shifts in position can be observed. This can be ascribed to the minute structural modifications due to mutual interactions. Because of amorphous structure of CQDs, low content and good dispersion no peaks are observed [43]. The XRD pattern confirms the successful formation of the heterojunction.

### 3.1.2 SEM and TEM analysis

Figure 3 (a-b) represents the SEM images of CCGV, showing the morphology. It can be seen that  $V_2O_5$  and  $CeO_2$  nanoparticles dispersed over thin  $g-C_3N_4$  nanosheets. On higher resolution, the semiconductor metal oxide nanoparticles can be seen in intimate contact with each other and with carbon nitride. The lighter colored and cubic nanoparticles represent  $CeO_2$  and darker spherical particles are the  $V_2O_5$ . The corresponding TEM images showing the microstructure of CCGV are presented in Figure 3 (c-d), in which the  $V_2O_5$  and  $CeO_2$  nanoparticles can be seen uniformly distributed over the  $g-C_3N_4$  matrix confirming the heterojunction structure. The intimate contact among all three can be seen. HRTEM image (Figure 3d) shows the three moieties in intimate interfacial contact with lattice fringes visible. The fringes and contact can be more clearly visible in the HRTEM image in Figure S1. The d-spacings, as calculated from the HRTEM image, agree with XRD results. SAED pattern (Figure 3e) shows the high crystallinity of the photocatalyst. The elemental mapping for CCGV can be seen in Figure 3(f-k). All the constituent elements are present in the material, and a uniform structure can be observed. Further elemental analysis is done by XPS measurements. Surface area measurements (Figure S2) show that  $N_2$  adsorption for CCGV

exhibits type-IV isotherm ( $H_4/H_3$  hybrid hysteresis) [44] with  $48.2 \text{ m}^2\text{g}^{-1}$  surface area. The pore size for CCGV is 19.23 nm and pore volume of  $0.22 \text{ cm}^3\text{g}^{-1}$ . The surface area is sufficiently high for high adsorption of Cr(VI) ions owing to the various possible adsorption sites.

### 3.1.3 XPS analysis

XPS analysis was further used for the analysis of chemical composition and surface oxidation state of the ternary heterojunction CCGV. The survey scan (Figure 4a) shows the peaks for all the constituent elements, i.e., V, C, N, O, and Ce confirming their presence in the material. The Ce 3d spectrum (Figure 4b) shows the deconvoluted peak at 883.1 eV, which can be ascribed to Ce(III)  $3d_{3/2}$  and at 900.7 eV refers to Ce(III)  $3d_{5/2}$ . Also the peak at 897.2 eV corresponds to Ce(IV)  $3d_{5/2}$  [45]. Figure 4 (c) shows the V 2p spectrum for  $\text{V}_2\text{O}_5$  exhibiting two typical peaks at 514.3 eV, 515.2 eV referring to  $\text{V}^{4+}$  and  $\text{V}^{5+}$  oxidation states ( $2p_{3/2}$ ) and the third peak at 524.5 eV is ascribed to the splitting of the  $\text{V}^{5+}$   $2p_{1/2}$  spin-orbital [46]. The O1s spectrum (Figure 4d) exhibits two peaks at 528.6 & 530.4 eV corresponding to oxygen from oxide and hydroxyl groups, respectively. The adsorbed OH groups on the catalyst surface are beneficial for the production of  $\bullet\text{OH}$  and  $\bullet\text{O}_2^-$  radicals during the irradiation process. The C 1s spectrum (Figure 4e) shows two peaks at 283.6 eV and 287.1 eV corresponding to  $\text{sp}^2$  C and N-C=N bonds of graphitic  $\text{C}_3\text{N}_4$ , respectively [47]. The deconvoluted N1s spectrum is shown in Figure 4 (f). The three peaks at 397.3, 398.2, and 399.3 eV are assigned to pyridine N ( $\text{sp}^2$ -bonded N) involved in the formation of triazine rings, i.e. (C=N-C), N-(C)<sub>3</sub> and N from (C-N-H) respectively [48]. The C1s peaks are shifted to slightly lower B.E. values as per literature [49], but the 284.6 eV standard carbon peak has not changed after junction formation with metal oxides. There have been slight changes in the binding energies from standard values of these bare semiconductors, and these shifts are an indicator of changes in surface charge densities, which can occur due to electron transfer between semiconductors.

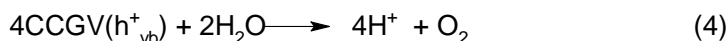
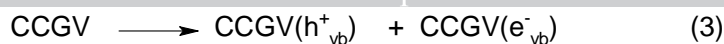
### 3.1.4 Optical and electrochemical studies

The UV-DRS spectra of  $V_2O_5$ ,  $CeO_2$ ,  $g-C_3N_4$  and CCGV were recorded results are shown in Figure 5(a). The  $g-C_3N_4$  shows visible absorption with a typical absorption edge near 450 nm. On the other hand,  $CeO_2$  has low visible absorption, and  $V_2O_5$  shows considerably high. With the junction formed between these three, the absorption edge shows a considerable redshift with the extension of absorption to the near infra-red region. The improved spectral response is because of dual Z-scheme hetero-junction formation [50] and the up-conversion effect of the CQDs. The bandgaps were measured from Tauc plots (Figure 5b). The bands as calculated are 3.1 eV, 2.7 eV, and 2.6 eV for  $CeO_2$ ,  $g-C_3N_4$ , and  $V_2O_5$ , respectively. The valence band edges for  $CeO_2$ ,  $g-C_3N_4$ , and  $V_2O_5$  are calculated as 2.03 eV, 3.68 eV, and 2.9 eV, respectively. The corresponding CB edges in the same order are -1.07 eV, 0.98 eV and 0.5 eV. As it can be observed that the VB and CB edges are such placed that there is easy diffusion of charge carriers along with the interfaces. To ascertain the reduced recombination in the ternary heterojunction photoluminescence (PL) was also performed. The results in Figure 5(c) show that the PL intensity order is:  $V_2O_5 > g-C_3N_4 > CeO_2 > CCGV$ .  $V_2O_5$  shows the highest photoluminescence because its bandgap is the lowest of the three components suggesting the highest recombination. The ternary junction CCGV shows the lowest recombination with the highest separation capacity. The dual Z-scheme transfer heterojunction formation among  $V_2O_5$ ,  $g-C_3N_4$  and  $CeO_2$  diminishes the recombination. The transfer of photogenerated electrons from CB of  $g-C_3N_4$  to VB of  $V_2O_5$  and  $CeO_2$  reduces the recombination in the semiconductors and increases the separation leading to poor photoluminescence. Also, CQDs ensure the dual Z-transfer and further reduce the recombination. Electrochemical impedance spectroscopy (EIS) was also performed on the electrochemical work station to test the electron transfer capacity and flow. Figure 5 (d) shows EIS Nyquist plots for single and ternary photocatalysts. The changes in electrochemical impedance in a hetero-structure actually indicates the changes in the

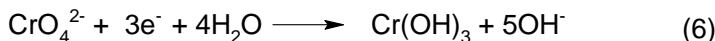
interfacial properties [51]. When the transfer of electrons occurs at the interfaces or along with the Fermi levels, the impedance gets reduced. This reduction is represented by a decreased arc radius in the Nyquist plots. As can be observed, the ternary junction CCGV shows the lowest radius, which indicates the best electron transfer and the least impedance.

### 3.2 Photo-reduction of Cr(VI)

To test the photocatalytic ability, several photo-reduction experiments were performed under a Xe lamp with a visible filter at optimized pH 2. The results are presented in Figure 6. Without any sacrificial agent (hole scavenging), the Cr(VI) to Cr(III) photo-reduction in 90 min visible light exposure the performance follows the order : CCGV (99.4%) > V<sub>2</sub>O<sub>5</sub> (62.6%) > g-C<sub>3</sub>N<sub>4</sub> (56.9%) > CeO<sub>2</sub> (17.5%). As expected, the CeO<sub>2</sub> bandgap of 3.1 eV shows the poorest performance because of limited absorption in visible light (Figure 6a). Followed by CeO<sub>2</sub>, g-C<sub>3</sub>N<sub>4</sub>, and V<sub>2</sub>O<sub>5</sub> shows improvement because of the low bandgap, but the performance is poor because of the high recombination rate. On the other hand, the ternary heterojunction performs exceptionally exhibiting an almost complete Cr<sup>6+</sup> removal within 90 min. Figure S3 shows the time-dependent absorption spectra of the DPC-Cr(VI) complex solution obtained by sampling from the reactor. It can be observed that the absorption peak at 540 nm (for complex) falls rapidly with the exposure time and almost disappears with time. The dual Z-scheme transfer and CQDs increase the visible absorption and reduce the recombination dramatically. A pseudo-first-order kinetics model was applied for reaction, and plots are shown in Figure 6(b). The rate constant order is CCGV (0.08122 min<sup>-1</sup>) > V<sub>2</sub>O<sub>5</sub> (0.03423 min<sup>-1</sup>) > g-C<sub>3</sub>N<sub>4</sub> (0.03122 min<sup>-1</sup>) > CeO<sub>2</sub> (0.01012 min<sup>-1</sup>). This shows that the photo-reduction rate is ~8 times faster than bare CeO<sub>2</sub>. The results are in accordance with UV-DRS, PL, and EIS results. On light irradiation, the holes-electrons pairs are generated, where electrons bring about the reduction of Cr<sup>6+</sup> to Cr<sup>3+</sup> (scheme 1, reactions 3-5) and the holes produce oxygen from water.



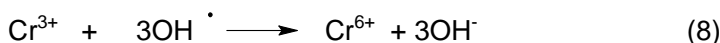
*In basic medium*



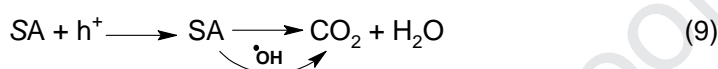
*In acidic medium*



Reaction with  $\text{OH}^\bullet$



*In presence of sacrificial agent (SA)*



**Scheme 1:** Various reactions during photo-reduction of Cr(VI) over CCGV

The electrons from CB of g-C<sub>3</sub>N<sub>4</sub> move to VB of V<sub>2</sub>O<sub>5</sub> and CeO<sub>2</sub> and high potential electrons at CB of V<sub>2</sub>O<sub>5</sub> and CeO<sub>2</sub> for effective photo-reduction of Cr(VI) (Figure 7). Also, CQDs absorb visible light to enhance the capture. They may also act as bridges to facilitate the Z-scheme transfer. As mentioned earlier, the pH was optimized for experiments and the best results were obtained at pH=2. The effect of pH onto Cr<sup>6+</sup> reduction by CCGV under visible light was tested (Figure 6c). The reactions are given in scheme 2, reactions 6-7. At acidic pH, the performance is better, the catalyst surface is positively charged, and HCrO<sub>4</sub><sup>-</sup> ions are dominant, which favors the interactions with the catalyst surface, and Cr(VI) gets rapidly reduced. However, the reduction falls at higher pH or neutral medium because of the dominance of CrO<sub>4</sub><sup>2-</sup> and negative charge on the catalyst surface, which leads to repulsions. Also, in alkaline medium, Cr(OH)<sub>3</sub> precipitates and deposits on the surface of the catalyst, thus, hampering the reduction [52].

### 3.2.1 Effect of operational parameters

In the water system, there are many common electrolytes or ions present, which may affect the photocatalytic reaction. Figure 6(d) displays the role of the most common electrolytes as  $\text{Ca}^{2+}$ ,  $\text{Cu}^{2+}$ ,  $\text{Na}^+$ ,  $\text{Mg}^{2+}$ ,  $\text{NO}_3^-$ ,  $\text{Cl}^-$ , and  $\text{SO}_4^{2-}$  on  $\text{Cr}^{6+}$  reduction over CCGV with visible light. As far as cations are concerned, no noticeable change is observed.  $\text{Na}^+$ ,  $\text{Mg}^{2+}$  &  $\text{Ca}^{2+}$  ions do not affect the rate while it falls slightly in the presence of  $\text{Cu}^{2+}$  ions, as they can scavenge photogenerated electrons [53]. Anions as  $\text{SO}_4^{2-}$  and  $\text{Cl}^-$  lead to an increase in the reduction capacity because they can scavenge the photogenerated holes and thus decrease the recombination. On the other hand,  $\text{NO}_3^-$  ions produce  $\bullet\text{OH}$  radicals under visible light [32], which can shift the equilibrium to the opposite side (scheme 1, equation 8). Further, the photocatalytic  $\text{Cr}^{6+}$  reduction was also tested under distilled water (DW) and municipal tap water (TW) to study the water matrix effect and applicability under real systems. Figure 6(d) shows that without any catalyst, no reduction is observed both in distilled and tap water. However, the degradation falls in tap water containing electrolytes and humic acid. However, the performance is not reduced to a great extent which means that catalyst is effective under natural water systems too.

### 3.2.2 Effect of sacrificial agents and scavengers

In the previous sections, it has been explained that the photogenerated electrons are responsible for the reduction of  $\text{Cr}^{6+}$  into  $\text{Cr}^{3+}$ . So some low weight organic acids and ethanol were added as sacrificial agents (SA), which accelerates the reduction by undergoing oxidation. For these experiments,  $10^{-4}$  mol of ethanol (EA), maleic acid (MA), and tartaric acid (TA) were used as SA. It is clearly visible that the rate increases manifolds with sacrificial agents. The fastest reduction is observed with TA with 100%  $\text{Cr}^{6+}$  removal in 30 min. The reaction rate follows the order:  $\text{TA} > \text{MA} > \text{EA} > \text{CCGV}$ . The role of sacrificial agents can be observed in equation 9. These acids scavenge holes and get oxidized and keep electrons free for reduction.

The number of -COOH and -OH groups influences the reactivity of sacrificial agents. TA has 2 OH groups and 2 carboxylic groups. This is followed by MA with 1 COOH group and ethanol with just 1 OH group. Because of the higher number of polar groups of TA, the Cr(VI) adsorption performance of CCGV is even improved. Further, KI, Ag<sup>+</sup>, and benzoquinone (BQ) were used for scavenging h<sup>+</sup>, e<sup>-</sup> and •O<sub>2</sub><sup>-</sup> respectively, from CCGV + visible system to assess the involved active species (Figure 8a). The photo-reduction efficiency markedly increased on the addition of KI, implying that on scavenging holes, the electrons are free for reduction. The addition of Ag<sup>+</sup> scavenges electrons, which decreases the rate. Hence, photogenerated electrons are primarily responsible for reduction, while •O<sub>2</sub><sup>-</sup> radicals are of secondary importance.

### 3.2.3 Photocatalytic mechanism, performance, and Reusability

The ternary junction CCGV shows remarkable photocatalytic activity, which is manifested in the Cr(VI) reduction results and supported by EIS and PL results. The wide spectral response, low impedance, reduced recombination, and electron flow is responsible for the remarkable activity of CCGV. Figure 7 shows the possible conventional heterojunction and dual Z-scheme heterojunction with the charge flow along with the bands. In the traditional ternary heterojunction, on irradiation, all the three semiconductors show transition and the e<sup>-</sup> from CB of V<sub>2</sub>O<sub>5</sub> (-1.07 eV) and CeO<sub>2</sub> (0.5 eV) migrate to CB of g-C<sub>3</sub>N<sub>4</sub> (0.98 eV). The h<sup>+</sup> from VB of g-C<sub>3</sub>N<sub>4</sub> (3.68 eV) migrate to VB of V<sub>2</sub>O<sub>5</sub> (2.03 eV) and that of CeO<sub>2</sub> (2.9 eV). The potential of electrons in CB of g-C<sub>3</sub>N<sub>4</sub> (0.98 eV) is higher than reduction potential E<sup>o</sup>[Cr(VI)/Cr(III)] = 0.51 eV [54]. This high potential brings about a rapid reduction of Cr(VI). The oxidation of H<sub>2</sub>O to O<sub>2</sub> will coincide with the VB of V<sub>2</sub>O<sub>5</sub> and CeO<sub>2</sub> having high potential than E<sup>o</sup>(H<sub>2</sub>O/O<sub>2</sub>)= 1.23 eV. Secondly, the formation of •O<sub>2</sub><sup>-</sup>, the second most active species, is not feasible by this traditional mechanism because CB of g-C<sub>3</sub>N<sub>4</sub> has not higher potential than E (O<sub>2</sub>/•O<sub>2</sub><sup>-</sup>) = -0.33 eV. However, hydroxyl radicals can still be

produced as VB potentials of both  $V_2O_5$  and  $CeO_2$  are highly positive than potential  $E(\cdot OH/H_2O)$  (2.27 eV) vs. NHE and  $E(\cdot OH/OH)$  (1.99 eV) [19]. By analysis of this conventional transfer mechanism, we do not expect faster or exceptional results.

Let us analyze the dual Z-scheme transfer mechanism. The photogenerated electrons in the CB of  $g-C_3N_4$  migrate to VB of  $V_2O_5$  and  $CeO_2$  as they are appropriately aligned. In addition, the presence of CQDs as bridges at each interface facilitates the migration of CB of  $g-C_3N_4$  to VB of the other two semiconductors. The route is  $g-C_3N_4 \rightarrow CQDs \rightarrow V_2O_5$  and  $g-C_3N_4 \rightarrow CQDs \rightarrow CeO_2$ . This makes the electrons in CB of  $V_2O_5$  and  $CeO_2$  free for reduction. The electrons in these two bands are highly negative than the required potential and also than  $g-C_3N_4$ .

Similarly, the CB potential of  $V_2O_5$  (-1.07 eV) is highly negative than  $E(O_2/\cdot O_2^-) = -0.33$  eV. Hence, as observed from scavenging experiments, the second active species present in the system is  $\cdot O_2^-$ . If we consider the traditional transfer mechanism, then the generation of  $\cdot O_2^-$  is not thermodynamically feasible, and its generation can only be explained by dual Z-scheme transfer. The rapid rate of reduction can only be explained only via dual Z-scheme transfer. Sacrificial agents like acids or ethanol, scavenge the holes and oxidizing OH radicals and speeding up the reduction process. The  $\cdot OH$  radicals tend to shift the Cr(VI)/Cr(III) equilibrium to the opposite side. In addition, these agents with polar groups form charge transfer complexes with the catalyst for better interaction and reduction.

The redshift in CCGV samples on account of bandgap lowering is attributed to the Z-scheme transfer of charge carriers and oxygen vacancies or defects on the CQDs or induced defects on catalysts by CQDs. The up-conversion properties of the carbon quantum dots help in high visible absorption and charge separation. With Fermi level located at -0.08 eV, which is more +ve than that of three semiconductors, a Schottky barrier can be easily formed between two intimate contacts, i.e.,  $g-C_3N_4-V_2O_5$  and  $CeO_2-g-C_3N_4$  via CQDs. This leads to the

migration of electrons and the shifting of the Fermi level. The oxygen vacancies on the catalyst surface induced by CQDs also contribute to the photocatalytic activity. These surface oxygen vacancies/defects trap electrons or holes and inhibit the recombination rate and also have a tendency to transfer the charge carriers to the catalyst as well as adsorbed pollutant species [55].

As photocatalyst shows a broad-spectrum response, the photo-reduction tests were also performed under natural sunlight and NIR light (Figure 8). Under sunlight, CCGV shows 78.2% Cr(VI) photo-reduction at pH=2, which increases to 90.2 % if TA is used as a sacrificial agent. These results show that the high photo-activity of CCGV catalysts is retained outdoors under the sun. However, the reaction is slower because of the lower energy of sunlight. Under NIR light, a 21.1% reduction is achieved, which is possible because of NIR absorbing capacity. The photocatalytic performance of CCGV as compared to other Z-scheme and dual Z-scheme heterojunctions is shown in Table 1. The results reveal that CCGV is a highly active photocatalyst active under a wide spectrum with excellent performance for Cr(VI) reduction. Also, the CQDs aid in the facile dual Z-scheme transfer for highly improved separation and extended absorption. Compared to similar or related junctions, this CCGV junction not only performs exceptional for photo-reductive performance but is also efficient under NIR light and natural solar light. The effectiveness of Z-scheme transfer is accelerated or routed by bridging materials as quantum dots (CQDS in this case). Thus, the heterojunction performs better than other dual Z-scheme materials because of the correct placing of Fermi levels of these quantum dots for faster transfer from CB to VB for maintaining high potential conduction bands.

**Table 1:** Comparative performance of Z-scheme and dual Z-scheme heterojunction photocatalysts for visible light Cr(VI) reduction

S.No	Photocatalyst	Cr(VI) concentration, pH	Catalyst dosage	Performance	Ref
1.	TiO <sub>2</sub> @C/CdS	20 mg L <sup>-1</sup>	0.6 mg mL <sup>-1</sup>	98.1% reduction in 50 min under visible light (300 W Xe lamp)	[56]
2.	Ag/Bi <sub>4</sub> O <sub>7</sub> /g-C <sub>3</sub> N <sub>4</sub>	50 mg L <sup>-1</sup> , pH = 3	0.3 mg mL <sup>-1</sup>	98% reduction in 60 min under visible light (300 W Xe lamp)	[57]
3.	V <sub>2</sub> O <sub>5</sub> /g-C <sub>3</sub> N <sub>4</sub>	20 mg L <sup>-1</sup> , pH = 2	0.1 mg mL <sup>-1</sup>	71% reduction within 90 min under sunlight	[58]
4.	CoS <sub>2</sub> /g-C <sub>3</sub> N <sub>4</sub> -rGO	20 mg L <sup>-1</sup> , pH=2	0.2 mg mL <sup>-1</sup>	99.8% reduction efficiency for Cr(VI) within 120 min (350 W Xe lamp)	[59]
5.	Cu <sub>2</sub> WS <sub>4</sub> /g-C <sub>3</sub> N <sub>4</sub>	10 mg L <sup>-1</sup>	0.5 mg mL <sup>-1</sup>	98.3% reduction in 100 min under visible light (300 W Xe lamp)	[60]
6.	ZnO-Fe <sub>2</sub> O <sub>3</sub>	20 mg L <sup>-1</sup> , pH = 2	0.4 mg mL <sup>-1</sup>	88% photo-reduction under visible light in 90 min (300 W Xe lamp)	[61]
7.	α-Fe <sub>2</sub> O <sub>3</sub> /g-C <sub>3</sub> N <sub>4</sub>	10 mg L <sup>-1</sup> , pH=2	2 mg mL <sup>-1</sup>	98% reduction in 120 min under visible light (300 W Xe lamp)	[62]
8.	g-C <sub>3</sub> N <sub>4</sub> /GO/BiFeO <sub>3</sub>	5 mg L <sup>-1</sup> , pH=2	2.5 mg mL <sup>-1</sup>	100% Cr(VI) removal within 120 min (300 W Xe lamp)	[63]
9.	SnO <sub>2</sub> /Bi <sub>2</sub> O <sub>3</sub> /BiOI	50 mg L <sup>-1</sup> , pH=3	0.5 mg mL <sup>-1</sup>	81.7% reduction in 120 min (500 W Xe lamp)	[64]
10.	GO/g-C <sub>3</sub> N <sub>4</sub> /MoS <sub>2</sub>	10 mg L <sup>-1</sup>	0.4 mg mL <sup>-1</sup>	~80% reduction in 120 min, (300 W Xe lamp)	[65]
11.	CQDs decorated CeO <sub>2</sub> /g-C <sub>3</sub> N <sub>4</sub> /V <sub>2</sub> O <sub>5</sub> (CCGV)	20 mg L <sup>-1</sup> , pH=2	0.3 mg mL <sup>-1</sup>	99% reduction in 100 min (300 W Xe lamp)	This study

After the reduction tests are over, XPS analysis of CCGV (catalyst + visible light + TA system) was performed to confirm the photo-reduction of Cr(VI) into Cr(III). The survey scan (Figure 8c) confirms that all the constituent elements are present with an additional peak of adsorbed Cr(III). The structure of the catalyst is not changed as no changes are

observed in the survey scan. The Cr 2p spectrum (Figure 8d) is deconvoluted further into two peaks at 576.9 and 586.5 eV, which are assigned to  $2p_{3/2}$  and  $2p_{1/2}$  for  $\text{Cr}^{3+}$ , respectively [66]. The complete conversion is confirmed as no peaks for Cr(VI) are present.

Further, the reusability studies for CCGV catalyst under the visible system are shown in Figure 8(d). There is no abnormal fall in the catalytic activity after five cycles. Thus, the catalyst is stable, reusable, and fully recoverable from the reaction system. The TEM image of CCGV (Figure 8e) shows that the microstructure of the catalyst does not change after use and recovery. Thus CQDs decorated  $\text{CeO}_2/\text{g-C}_3\text{N}_4/\text{V}_2\text{O}_5$ /ternary nano hetero-structures are an efficient and wide spectrum photocatalytic material with a dual Z-scheme mechanism for rapid Cr(VI) reduction. CCGV works efficiently under natural sunlight, tap water and is promising for photocatalysis based environmental remediation and energy production.

#### 4. Conclusions

In summary, CQDs decorated  $\text{CeO}_2/\text{g-C}_3\text{N}_4/\text{V}_2\text{O}_5$  ternary heterojunction (CCGV) with a dual Z-scheme transfer of electrons has been prepared by a simple technique. UV-DRS, PL, and EIS results reveal that the CCGV catalyst shows a wide spectral response extending up to the NIR region, with low recombination and high charge transfer capacity. The ternary heterojunction displayed remarkable photocatalytic activity with 99.4%  $\text{Cr}^{6+}$  reduction in 90 min without any sacrificial agent. The catalyst shows an eightfold higher rate than bare  $\text{CeO}_2$ . The enhanced  $\text{Cr}^{6+}$  reduction with CCGV is mainly ascribed to improved visible absorption capacity, accelerated charge transfer, and restrained recombination rate. Also, the high protected energy bands via Z-scheme transfer and up-conversion by CQDs facilitate the charge transfer and generation of high energy reactive oxygen species. The role of dominant oxygen species was also examined by scavenging experiments, which reveal that photogenerated electrons are the main species followed by  $\bullet\text{O}_2^-$ . The excellent performance was explained in terms of possibilities of traditional double charge transfer mechanism and

dual Z-scheme transfer. By analysis of band structure and thermodynamic feasibility of reactive oxygen species, it was found that dual Z-scheme transfer facilitated by CQDs is responsible for high photo-reductive capabilities.

### **Declaration of Competing Interest**

The authors declare that they have no known competing financial interests or personal relationships that could have appeared to influence the work reported in this paper.

### **Acknowledgments**

One of the authors (M. Naushad) is grateful to the Researchers Supporting Project number (RSP-2019/8), King Saud University, Riyadh, Saudi Arabia for funding this research.

### **References**

- [1] R. Zhang, Q. Han, Y. Li, T. Zhang, Y. Liu, K. Zeng, C. Zhao, Solvothermal synthesis of a peony flower-like dual Z-scheme PANI/BiOBr/ZnFe<sub>2</sub>O<sub>4</sub> photocatalyst with excellent photocatalytic redox activity for organic pollutant under visible-light, *Separation and Purification Technology*, 234 (2020) 116098.
- [2] S. Zarrin, F. Heshmatpour, Photocatalytic activity of TiO<sub>2</sub>/Nb<sub>2</sub>O<sub>5</sub>/PANI and TiO<sub>2</sub>/Nb<sub>2</sub>O<sub>5</sub>/RGO as new nanocomposites for degradation of organic pollutants, *Journal of Hazardous Materials*, 351 (2018) 147-159.
- [3] W.H. Organization, Potable reuse: guidance for producing safe drinking-water, (2017).
- [4] A. Kumar, G. Sharma, M. Naushad, A.a.H. Al-Muhtaseb, A. García-Peñas, G.T. Mola, C. Si, F.J. Stadler, Bio-inspired and biomaterials-based hybrid photocatalysts for environmental detoxification: A review, *Chemical Engineering Journal*, 382 (2020) 122937.
- [5] A. Priyadharsan, V. Vasanthakumar, S. Karthikeyan, V. Raj, S. Shanavas, P.M. Anbarasan, Multi-functional properties of ternary CeO<sub>2</sub>/SnO<sub>2</sub>/rGO nanocomposites: Visible light driven photocatalyst and heavy metal removal, *Journal of Photochemistry and Photobiology A: Chemistry*, 346 (2017) 32-45.
- [6] Y. Guo, Y. Yang, X. Yin, J. Zhao, Y. Han, J. Liu, W. Chen, M. Que, J. Zhang, W. Que, Heavy metal waste treatment product as semiconductor: Efficient visible light photocatalytic activity of the Bismuth(III) chelates, *Journal of Alloys and Compounds*, 774 (2019) 75-81.

- [7] G. Sharma, M. Naushad, D. Pathania, A. Kumar, A multifunctional nanocomposite pectin thorium(IV) tungstomolybdate for heavy metal separation and photoremediation of malachite green, *Desalination and Water Treatment*, 57 (2016) 19443-19455.
- [8] X. Tian, M. Liu, K. Iqbal, W. Ye, Y. Chang, Facile synthesis of nitrogen-doped carbon coated  $\text{Fe}_3\text{O}_4/\text{Pd}$  nanoparticles as a high-performance catalyst for Cr (VI) reduction, *Journal of Alloys and Compounds*, (2020) 154059.
- [9] A. Kumar, C. Guo, G. Sharma, D. Pathania, M. Naushad, S. Kalia, P. Dhiman, Magnetically recoverable  $\text{ZrO}_2/\text{Fe}_3\text{O}_4/\text{chitosan}$  nanomaterials for enhanced sunlight driven photoreduction of carcinogenic Cr (VI) and dechlorination & mineralization of 4-chlorophenol from simulated waste water, *RSC Advances*, 6 (2016) 13251-13263.
- [10] M.K. Guria, A.K. Guha, M. Bhattacharyya, A green chemical approach for biotransformation of Cr(VI) to Cr(III), utilizing *Fusarium* sp. MMT1 and consequent structural alteration of cell morphology, *Journal of Environmental Chemical Engineering*, 2 (2014) 424-433.
- [11] X.-H. Yi, S.-Q. Ma, X.-D. Du, C. Zhao, H. Fu, P. Wang, C.-C. Wang, The facile fabrication of 2D/3D Z-scheme  $\text{g-C}_3\text{N}_4/\text{UiO-66}$  heterojunction with enhanced photocatalytic Cr(VI) reduction performance under white light, *Chemical Engineering Journal*, 375 (2019) 121944.
- [12] A. Kumar, S.K. Sharma, G. Sharma, A.a.H. Al-Muhtaseb, M. Naushad, A.A. Ghfar, F.J. Stadler, Wide spectral degradation of Norfloxacin by  $\text{Ag@BiPO}_4/\text{BiOBr}/\text{BiFeO}_3$  nano-assembly: Elucidating the photocatalytic mechanism under different light sources, *Journal of Hazardous Materials*, 364 (2019) 429-440.
- [13] S. S, A. Priyadharsan, E.I. Gkanas, R. Acevedo, P.M. Anbarasan, High efficient catalytic degradation of tetracycline and ibuprofen using visible light driven novel  $\text{Cu}/\text{Bi}_2\text{Ti}_2\text{O}_7/\text{rGO}$  nanocomposite: Kinetics, intermediates and mechanism, *Journal of Industrial and Engineering Chemistry*, 72 (2019) 512-528.
- [14] G. Sharma, V.K. Gupta, S. Agarwal, S. Bhogal, M. Naushad, A. Kumar, F.J. Stadler, Fabrication and characterization of trimetallic nano-photocatalyst for remediation of ampicillin antibiotic, *Journal of Molecular Liquids*, 260 (2018) 342-350.
- [15] A. Kumar, Shalini, G. Sharma, M. Naushad, A. Kumar, S. Kalia, C. Guo, G.T. Mola, Facile hetero-assembly of superparamagnetic  $\text{Fe}_3\text{O}_4/\text{BiVO}_4$  stacked on biochar for solar photo-degradation of methyl paraben and pesticide removal from soil, *Journal of Photochemistry and Photobiology A: Chemistry*, 337 (2017) 118-131.

- [16] A. Kumar, A. Kumar, G. Sharma, M. Naushad, F.J. Stadler, A.A. Ghfar, P. Dhiman, R.V. Saini, Sustainable nano-hybrids of magnetic biochar supported g-C<sub>3</sub>N<sub>4</sub>/FeVO<sub>4</sub> for solar powered degradation of noxious pollutants- Synergism of adsorption, photocatalysis & photo-ozonation, *Journal of Cleaner Production*, 165 (2017) 431-451.
- [17] M.A. Alcudia-Ramos, M.O. Fuentes-Torres, F. Ortiz-Chi, C.G. Espinosa-González, N. Hernández-Como, D.S. García-Zaleta, M.K. Kesarla, J.G. Torres-Torres, V. Collins-Martínez, S. Godavarthi, Fabrication of g-C<sub>3</sub>N<sub>4</sub>/TiO<sub>2</sub> heterojunction composite for enhanced photocatalytic hydrogen production, *Ceramics International*, 46 (2020) 38-45.
- [18] H. Qin, K. Wang, L. Jiang, J. Li, X. Wu, G. Zhang, Ultrasonic-assisted fabrication of a direct Z-scheme BiOI/Bi<sub>2</sub>O<sub>4</sub> heterojunction with superior visible light-responsive photocatalytic performance, *Journal of Alloys and Compounds*, 821 (2020) 153417.
- [19] W.-K. Jo, T.S. Natarajan, Fabrication and efficient visible light photocatalytic properties of novel zinc indium sulfide (ZnIn<sub>2</sub>S<sub>4</sub>) – graphitic carbon nitride (g-C<sub>3</sub>N<sub>4</sub>)/bismuth vanadate (BiVO<sub>4</sub>) nanorod-based ternary nanocomposites with enhanced charge separation via Z-scheme transfer, *Journal of Colloid and Interface Science*, 482 (2016) 58-72.
- [20] M. Rauf, S. Bukallah, A. Hamadi, A. Sulaiman, F. Hammadi, The effect of operational parameters on the photoinduced decoloration of dyes using a hybrid catalyst V<sub>2</sub>O<sub>5</sub>/TiO<sub>2</sub>, *Chemical Engineering Journal*, 129 (2007) 167-172.
- [21] K. Teramura, T. Tanaka, M. Kani, T. Hosokawa, T. Funabiki, Selective photo-oxidation of neat cyclohexane in the liquid phase over V<sub>2</sub>O<sub>5</sub>/Al<sub>2</sub>O<sub>3</sub>, *Journal of Molecular Catalysis A: Chemical*, 208 (2004) 299-305.
- [22] W. Liu, J. Zhou, J. Yao, Shuttle-like CeO<sub>2</sub>/g-C<sub>3</sub>N<sub>4</sub> composite combined with persulfate for the enhanced photocatalytic degradation of norfloxacin under visible light, *Ecotoxicology and Environmental Safety*, 190 (2020) 110062.
- [23] G.B. Vieira, H.J. José, M. Peterson, V.Z. Baldissarelli, P. Alvarez, R. de Fátima Peralta Muniz Moreira, CeO<sub>2</sub>/TiO<sub>2</sub> nanostructures enhance adsorption and photocatalytic degradation of organic compounds in aqueous suspension, *Journal of Photochemistry and Photobiology A: Chemistry*, 353 (2018) 325-336.
- [24] J. Shen, J. Shen, W. Zhang, X. Yu, H. Tang, M. Zhang, Zulfiqar, Q. Liu, Built-in electric field induced CeO<sub>2</sub>/Ti<sub>3</sub>C<sub>2</sub>-MXene Schottky-junction for coupled photocatalytic tetracycline degradation and CO<sub>2</sub> reduction, *Ceramics International*, 45 (2019) 24146-24153.
- [25] D. Sharma, V.R. Satsangi, R. Shrivastav, U.V. Waghmare, S. Dass, Understanding the photoelectrochemical properties of nanostructured CeO<sub>2</sub>/Cu<sub>2</sub>O heterojunction photoanode for

efficient photoelectrochemical water splitting, *International Journal of Hydrogen Energy*, 41 (2016) 18339-18350.

[26] S. Shanavas, A. Priyadharsan, V. Vasanthakumar, A. Arunkumar, P.M. Anbarasan, S. Bharathkumar, Mechanistic investigation of visible light driven novel  $\text{La}_2\text{CuO}_4/\text{CeO}_2/\text{rGO}$  ternary hybrid nanocomposites for enhanced photocatalytic performance and antibacterial activity, *Journal of Photochemistry and Photobiology A: Chemistry*, 340 (2017) 96-108.

[27] J. Singh, A. Arora, S. Basu, Synthesis of coral like  $\text{WO}_3/\text{g-C}_3\text{N}_4$  nanocomposites for the removal of hazardous dyes under visible light, *Journal of Alloys and Compounds*, 808 (2019) 151734.

[28] J. Bai, W. Lv, Z. Ni, Z. Wang, G. Chen, H. Xu, H. Qin, Z. Zheng, X. Li, Integrating  $\text{MoS}_2$  on sulfur-doped porous  $\text{g-C}_3\text{N}_4$  iostype heterojunction hybrids enhances visible-light photocatalytic performance, *Journal of Alloys and Compounds*, 768 (2018) 766-774.

[29] P. Yang, J. Wang, G. Yue, R. Yang, P. Zhao, L. Yang, X. Zhao, D. Astruc, Constructing mesoporous  $\text{g-C}_3\text{N}_4/\text{ZnO}$  nanosheets catalyst for enhanced visible-light driven photocatalytic activity, *Journal of Photochemistry and Photobiology A: Chemistry*, 388 (2020) 112169.

[30] Y. Zhou, W. Lv, B. Zhu, F. Tong, J. Pan, J. Bai, Q. Zhou, H. Qin, Template-Free One-Step Synthesis of  $\text{g-C}_3\text{N}_4$  Nanosheets with Simultaneous Porous Network and S-Doping for Remarkable Visible-Light-Driven Hydrogen Evolution, *ACS Sustainable Chemistry & Engineering*, 7 (2019) 5801-5807.

[31] S. Kang, M. He, M. Chen, Y. Liu, Y. Wang, Y. Wang, M. Dong, X. Chang, L. Cui, Surface Amino Group Regulation and Structural Engineering of Graphitic Carbon Nitride with Enhanced Photocatalytic Activity by Ultrafast Ammonia Plasma Immersion Modification, *ACS Applied Materials & Interfaces*, 11 (2019) 14952-14959.

[32] A. Kumar, A. Rana, G. Sharma, M. Naushad, A.a.H. Al-Muhtaseb, C. Guo, A. Iglesias-Juez, F.J. Stadler, High-Performance Photocatalytic Hydrogen Production and Degradation of Levofloxacin by Wide Spectrum-Responsive  $\text{Ag}/\text{Fe}_3\text{O}_4$  Bridged  $\text{SrTiO}_3/\text{g-C}_3\text{N}_4$  Plasmonic Nanojunctions: Joint Effect of Ag and  $\text{Fe}_3\text{O}_4$ , *ACS Applied Materials & Interfaces*, 10 (2018) 40474-40490.

[33] S. Shanavas, S. Mohana Roopan, A. Priyadharsan, D. Devipriya, S. Jayapandi, R. Acevedo, P.M. Anbarasan, Computationally guided synthesis of (2D/3D/2D)  $\text{rGO}/\text{Fe}_2\text{O}_3/\text{g-C}_3\text{N}_4$  nanostructure with improved charge separation and transportation efficiency for degradation of pharmaceutical molecules, *Applied Catalysis B: Environmental*, 255 (2019) 117758.

- [34] J. Kang, C. Jin, Z. Li, M. Wang, Z. Chen, Y. Wang, Dual Z-scheme  $\text{MoS}_2/\text{g-C}_3\text{N}_4/\text{Bi}_{24}\text{O}_{31}\text{Cl}_{10}$  ternary heterojunction photocatalysts for enhanced visible-light photodegradation of antibiotic, *Journal of Alloys and Compounds*, 825 (2020) 153975.
- [35] H. Yu, D. Wang, B. Zhao, Y. Lu, X. Wang, S. Zhu, W. Qin, M. Huo, Enhanced photocatalytic degradation of tetracycline under visible light by using a ternary photocatalyst of  $\text{Ag}_3\text{PO}_4/\text{AgBr}/\text{g-C}_3\text{N}_4$  with dual Z-scheme heterojunction, *Separation and Purification Technology*, 237 (2020) 116365.
- [36] J. Zhang, Z. Zhu, J. Jiang, H. Li, Fabrication of a novel  $\text{AgI}/\text{LaFeO}_3/\text{g-C}_3\text{N}_4$  dual Z-scheme photocatalyst with enhanced photocatalytic performance, *Materials Letters*, 262 (2020) 127029.
- [37] J. Huang, L. Li, J. Chen, F. Ma, Y. Yu, Broad spectrum response flower spherical-like composites  $\text{CQDs}@ \text{CdIn}_2\text{S}_4/\text{CdS}$  modified by CQDs with up-conversion property for photocatalytic degradation and water splitting, *International Journal of Hydrogen Energy*, 45 (2020) 1822-1836.
- [38] G. Sharma, S. Bhogal, M. Naushad, Inamuddin, A. Kumar, F.J. Stadler, Microwave assisted fabrication of  $\text{La}/\text{Cu}/\text{Zr}/\text{carbon dots}$  trimetallic nanocomposites with their adsorptional vs photocatalytic efficiency for remediation of persistent organic pollutants, *Journal of Photochemistry and Photobiology A: Chemistry*, 347 (2017) 235-243.
- [39] P. Dhiman, M. Naushad, K.M. Batoo, A. Kumar, G. Sharma, A.A. Ghfar, G. Kumar, M. Singh, Nano  $\text{Fe}_x\text{Zn}_{1-x}\text{O}$  as a tuneable and efficient photocatalyst for solar powered degradation of bisphenol A from aqueous environment, *Journal of Cleaner Production*, 165 (2017) 1542-1556.
- [40] Y. Xu, H. Xu, J. Yan, H. Li, L. Huang, J. Xia, S. Yin, H. Shu, A plasmonic photocatalyst of  $\text{Ag}/\text{AgBr}$  nanoparticles coupled with  $\text{g-C}_3\text{N}_4$  with enhanced visible-light photocatalytic ability, *Colloids and Surfaces A: Physicochemical and Engineering Aspects*, 436 (2013) 474-483.
- [41] A. Patterson, The Scherrer formula for X-ray particle size determination, *Physical review*, 56 (1939) 978.
- [42] V. Jayaraman, D. Sarkar, R. Rajendran, B. Palanivel, C. Ayappan, M. Chellamuthu, A. Mani, Synergistic effect of band edge potentials on  $\text{BiFeO}_3/\text{V}_2\text{O}_5$  composite: Enhanced photocatalytic activity, *Journal of Environmental Management*, 247 (2019) 104-114.
- [43] A. Aghamali, M. Khosravi, H. Hamishehkar, N. Modirshahla, M.A. Behnajady, Preparation of novel high performance recoverable and natural sunlight-driven

nanocomposite photocatalyst of  $\text{Fe}_3\text{O}_4/\text{C}/\text{TiO}_2/\text{N-CQDs}$ , *Materials Science in Semiconductor Processing*, 87 (2018) 142-154.

[44] Y. Yang, H. Zhao, H. Yang, P. Qiu, B. Zhou, N. Zhang, In situ fabrication of reduced graphene oxide/mesoporous g- $\text{C}_3\text{N}_4$  nanosheets with excellent visible light activity, *Journal of Environmental Chemical Engineering*, 6 (2018) 890-897.

[45] M. Li, F. Liu, Z. Ma, W. Liu, J. Liang, M. Tong, Different mechanisms for *E. coli* disinfection and BPA degradation by  $\text{CeO}_2\text{-AgI}$  under visible light irradiation, *Chemical Engineering Journal*, 371 (2019) 750-758.

[46] G. Huang, P. Guo, J. Wang, S. Chen, J. Liang, R. Tao, S. Tang, X. Zhang, S. Cheng, Y.-C. Cao, S. Dai, Lithiophilic  $\text{V}_2\text{O}_5$  nanobelt arrays decorated 3D framework hosts for highly stable composite lithium metal anodes, *Chemical Engineering Journal*, 384 (2020) 123313.

[47] Y. Shubin, G. Yongji, Z. Jinshui, Z. Liang, M. Lulu, F. Zheyu, V. Robert, W. Xinchun, A.P. M., Exfoliated Graphitic Carbon Nitride Nanosheets as Efficient Catalysts for Hydrogen Evolution Under Visible Light, *Advanced Materials*, 25 (2013) 2452-2456.

[48] A. Kumar, A. Kumari, G. Sharma, M. Naushad, T. Ahamad, F.J. Stadler, Utilizing recycled  $\text{LiFePO}_4$  from batteries in combination with  $\text{B@C}_3\text{N}_4$  and  $\text{CuFe}_2\text{O}_4$  as sustainable nano-junctions for high performance degradation of atenolol, *Chemosphere*, 209 (2018) 457-469.

[49] W. Iqbal, L. Wang, X. Tan, J. Zhang, One-step in situ green template mediated porous graphitic carbon nitride for efficient visible light photocatalytic activity, *Journal of Environmental Chemical Engineering*, 5 (2017) 3500-3507.

[50] Q. Li, N. Zhang, Y. Yang, G. Wang, D.H. Ng, High efficiency photocatalysis for pollutant degradation with  $\text{MoS}_2/\text{C}_3\text{N}_4$  hetero-structures, *Langmuir*, 30 (2014) 8965-8972.

[51] C. Zhou, C. Lai, P. Xu, G. Zeng, D. Huang, C. Zhang, M. Cheng, L. Hu, J. Wan, Y. Liu, W. Xiong, Y. Deng, M. Wen, In Situ Grown  $\text{AgI}/\text{Bi}_{12}\text{O}_{17}\text{Cl}_2$  Heterojunction Photocatalysts for Visible Light Degradation of Sulfamethazine: Efficiency, Pathway, and Mechanism, *ACS Sustainable Chemistry & Engineering*, 6 (2018) 4174-4184.

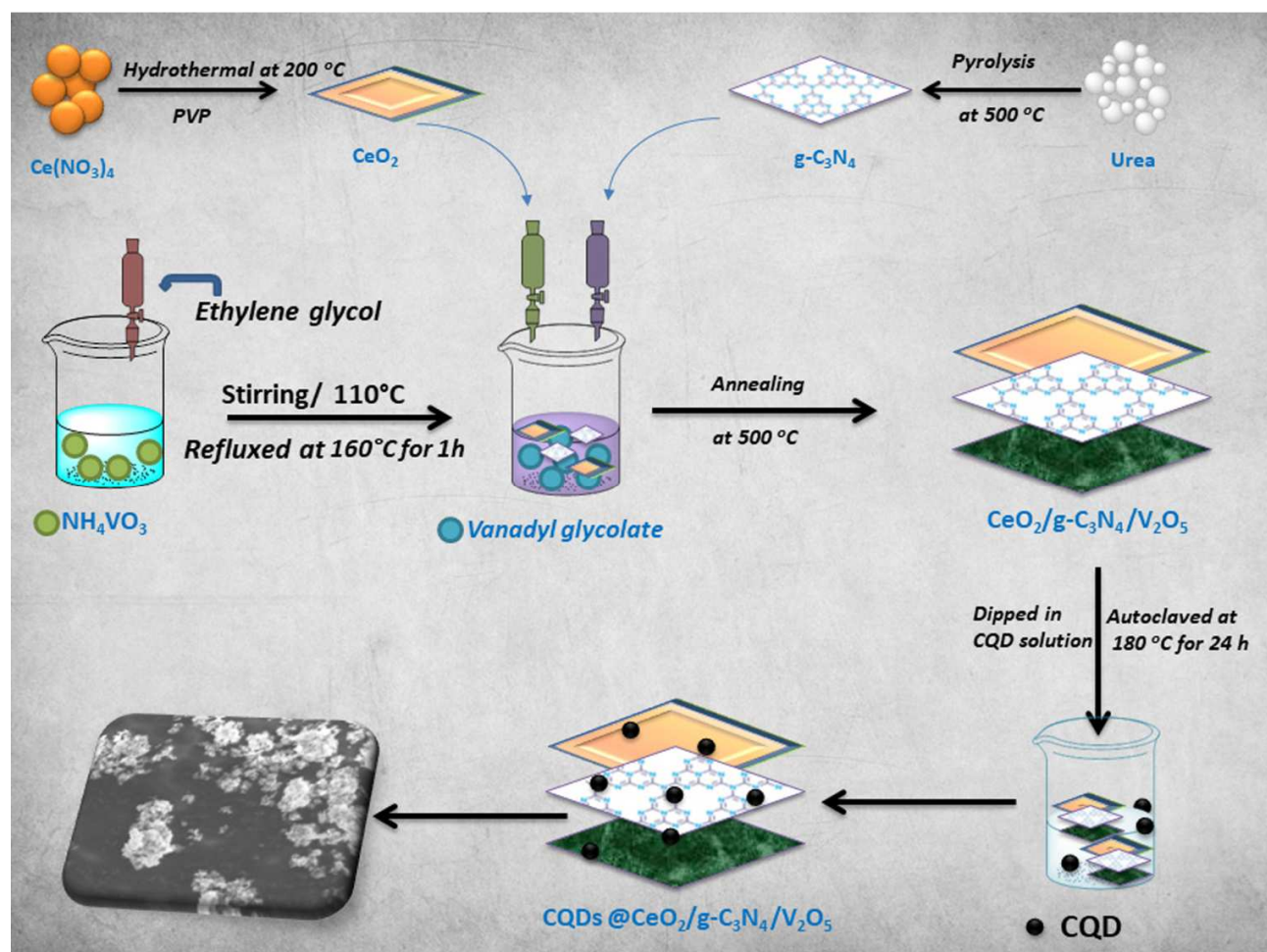
[52] C. Mondal, M. Ganguly, J. Pal, A. Roy, J. Jana, T. Pal, Morphology Controlled Synthesis of  $\text{SnS}_2$  Nanomaterial for Promoting Photocatalytic Reduction of Aqueous  $\text{Cr(VI)}$  under Visible Light, *Langmuir*, 30 (2014) 4157-4164.

[53] X. Zhao, S. Huang, Y. Liu, Q. Liu, Y. Zhang, In situ preparation of highly stable polyaniline/ $\text{W}_{18}\text{O}_{49}$  hybrid nanocomposite as efficient visible light photocatalyst for aqueous  $\text{Cr(VI)}$  reduction, *Journal of Hazardous Materials*, 353 (2018) 466-475.

- [54] B. Liu, X. Liu, L. Li, J. Li, C. Li, Y. Gong, L. Niu, X. Zhao, C.Q. Sun, ZnIn<sub>2</sub>S<sub>4</sub> flowerlike microspheres embedded with carbon quantum dots for efficient photocatalytic reduction of Cr(VI), *Chinese Journal of Catalysis*, 39 (2018) 1901-1909.
- [55] F. Duo, Y. Wang, C. Fan, X. Zhang, Y. Wang, Enhanced visible light photocatalytic activity and stability of CQDs/BiOBr composites: The upconversion effect of CQDs, *Journal of Alloys and Compounds*, 685 (2016) 34-41.
- [56] H. Yin, Y. Cao, T. Fan, B. Qiu, M. Zhang, J. Yao, P. Li, X. Liu, S. Chen, Construction of carbon bridged TiO<sub>2</sub>/CdS tandem Z-scheme heterojunctions toward efficient photocatalytic antibiotic degradation and Cr (VI) reduction, *Journal of Alloys and Compounds*, 824 (2020) 153915.
- [57] M. Ye, W. Wei, L. Zheng, Y. Liu, D. Wu, X. Gu, A. Wei, Enhanced visible light photoreduction of aqueous Cr(VI) by Ag/Bi<sub>4</sub>O<sub>7</sub>/g-C<sub>3</sub>N<sub>4</sub> nanosheets ternary metal/non-metal Z-scheme heterojunction, *Journal of Hazardous Materials*, 365 (2019) 674-683.
- [58] R. Dadigala, R. Bandi, B.R. Gangapuram, A. Dasari, H.H. Belay, V. Guttena, Fabrication of novel 1D/2D V<sub>2</sub>O<sub>5</sub>/g-C<sub>3</sub>N<sub>4</sub> composites as Z-scheme photocatalysts for CR degradation and Cr (VI) reduction under sunlight irradiation, *Journal of Environmental Chemical Engineering*, 7 (2019) 102822.
- [59] Y. Wang, S. Bao, Y. Liu, W. Yang, Y. Yu, M. Feng, K. Li, Efficient photocatalytic reduction of Cr(VI) in aqueous solution over CoS<sub>2</sub>/g-C<sub>3</sub>N<sub>4</sub>-rGO nanocomposites under visible light, *Applied Surface Science*, 510 (2020) 145495.
- [60] H. Che, G. Che, P. Zhou, C. Liu, H. Dong, Yeast-derived carbon sphere as a bridge of charge carriers towards to enhanced photocatalytic activity of 2D/2D Cu<sub>2</sub>WS<sub>4</sub>/g-C<sub>3</sub>N<sub>4</sub> heterojunction, *Journal of Colloid and Interface Science*, 546 (2019) 262-275.
- [61] P. Dhiman, S. Sharma, A. Kumar, M. Shekh, G. Sharma, M. Naushad, Rapid visible and solar photocatalytic Cr(VI) reduction and electrochemical sensing of dopamine using solution combustion synthesized ZnO-Fe<sub>2</sub>O<sub>3</sub> nano heterojunctions: Mechanism Elucidation, *Ceramics International*, (2020).
- [62] D. Xiao, K. Dai, Y. Qu, Y. Yin, H. Chen, Hydrothermal synthesis of  $\alpha$ -Fe<sub>2</sub>O<sub>3</sub>/g-C<sub>3</sub>N<sub>4</sub> composite and its efficient photocatalytic reduction of Cr(VI) under visible light, *Applied Surface Science*, 358 (2015) 181-187.
- [63] X. Hu, W. Wang, G. Xie, H. Wang, X. Tan, Q. Jin, D. Zhou, Y. Zhao, Ternary assembly of g-C<sub>3</sub>N<sub>4</sub>/graphene oxide sheets /BiFeO<sub>3</sub> heterojunction with enhanced photoreduction of Cr(VI) under visible-light irradiation, *Chemosphere*, 216 (2019) 733-741.

- [64] K. Wang, Z. Qian, W. Guo, Multi-heterojunction of SnO<sub>2</sub>/Bi<sub>2</sub>O<sub>3</sub>/BiOI nanofibers: Facile fabrication with enhanced visible-light photocatalytic performance, *Materials Research Bulletin*, 111 (2019) 202-211.
- [65] M.-h. Wu, L. Li, Y.-c. Xue, G. Xu, L. Tang, N. Liu, W.-y. Huang, Fabrication of ternary GO/g-C<sub>3</sub>N<sub>4</sub>/MoS<sub>2</sub> flower-like heterojunctions with enhanced photocatalytic activity for water remediation, *Applied Catalysis B: Environmental*, 228 (2018) 103-112.
- [66] Q. Yuan, L. Chen, M. Xiong, J. He, S.-L. Luo, C.-T. Au, S.-F. Yin, Cu<sub>2</sub>O/BiVO<sub>4</sub> heterostructures: synthesis and application in simultaneous photocatalytic oxidation of organic dyes and reduction of Cr(VI) under visible light, *Chemical Engineering Journal*, 255 (2014) 394-402.

Journal Pre-proof

**Figure 1: Synthesis Scheme**

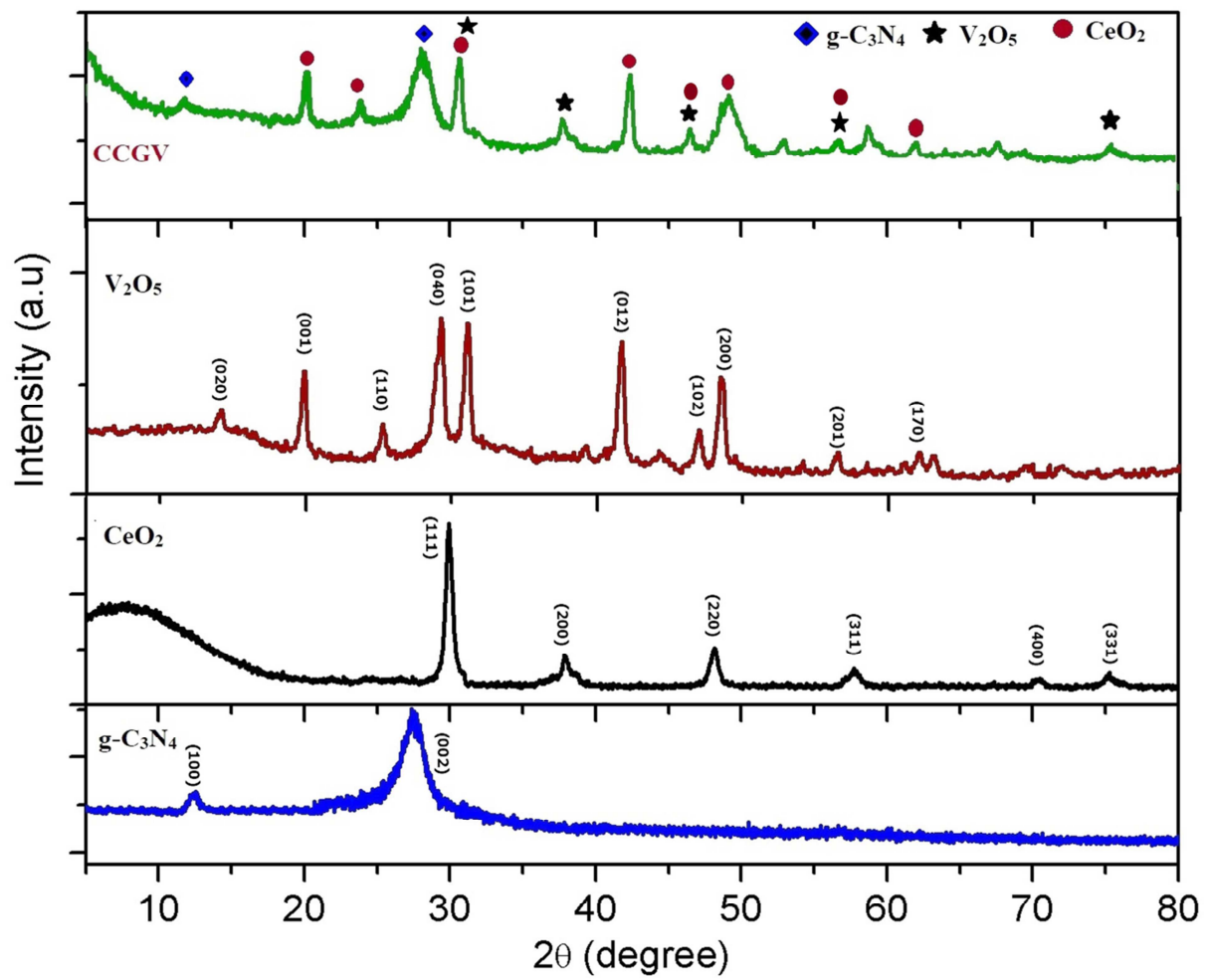
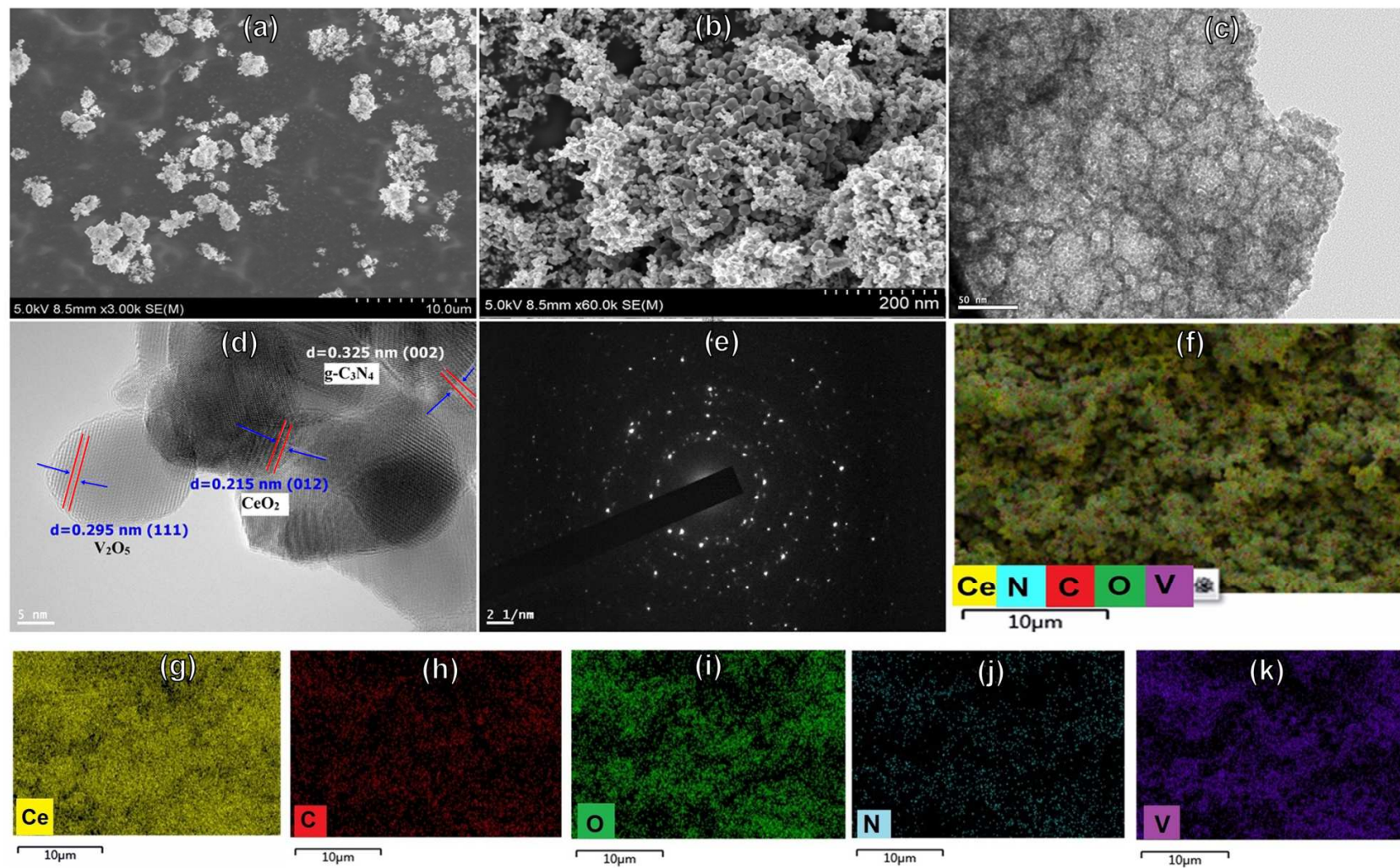
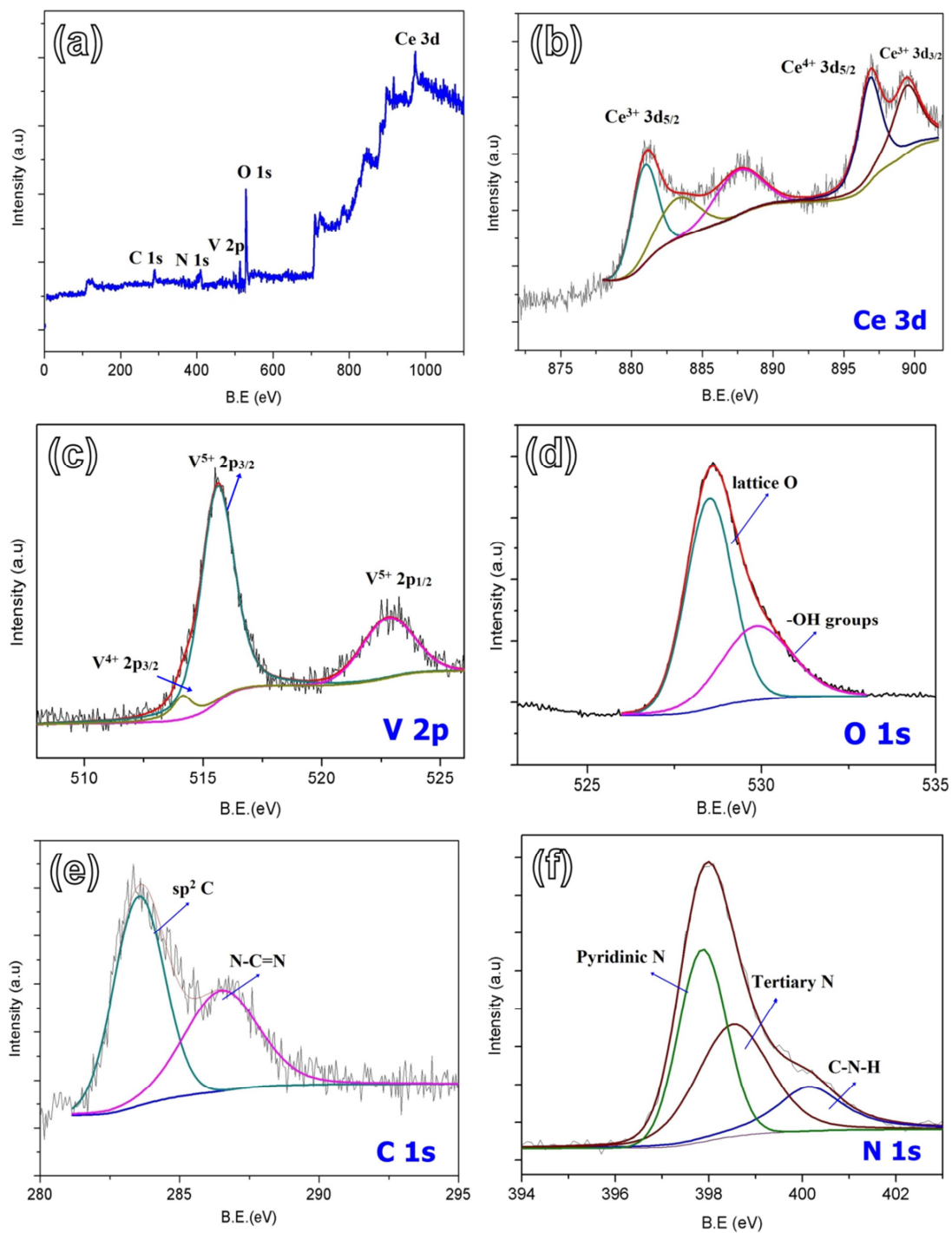


Figure 2: XRD pattern of synthesized photocatalyst



**Figure 3:** (a-b) SEM images of CCGV (c) TEM image of CCGV (d) HRTEM image (e) Corresponding SAED pattern (f-k) elemental mapping for CCGV



**Figure 4:** (a) XPS Survey scan for CCGV; Deconvoluted spectra for CCGV (b) Ce 3d (c) V 2p (d) O 1s (e) C 1s (f) N 1s

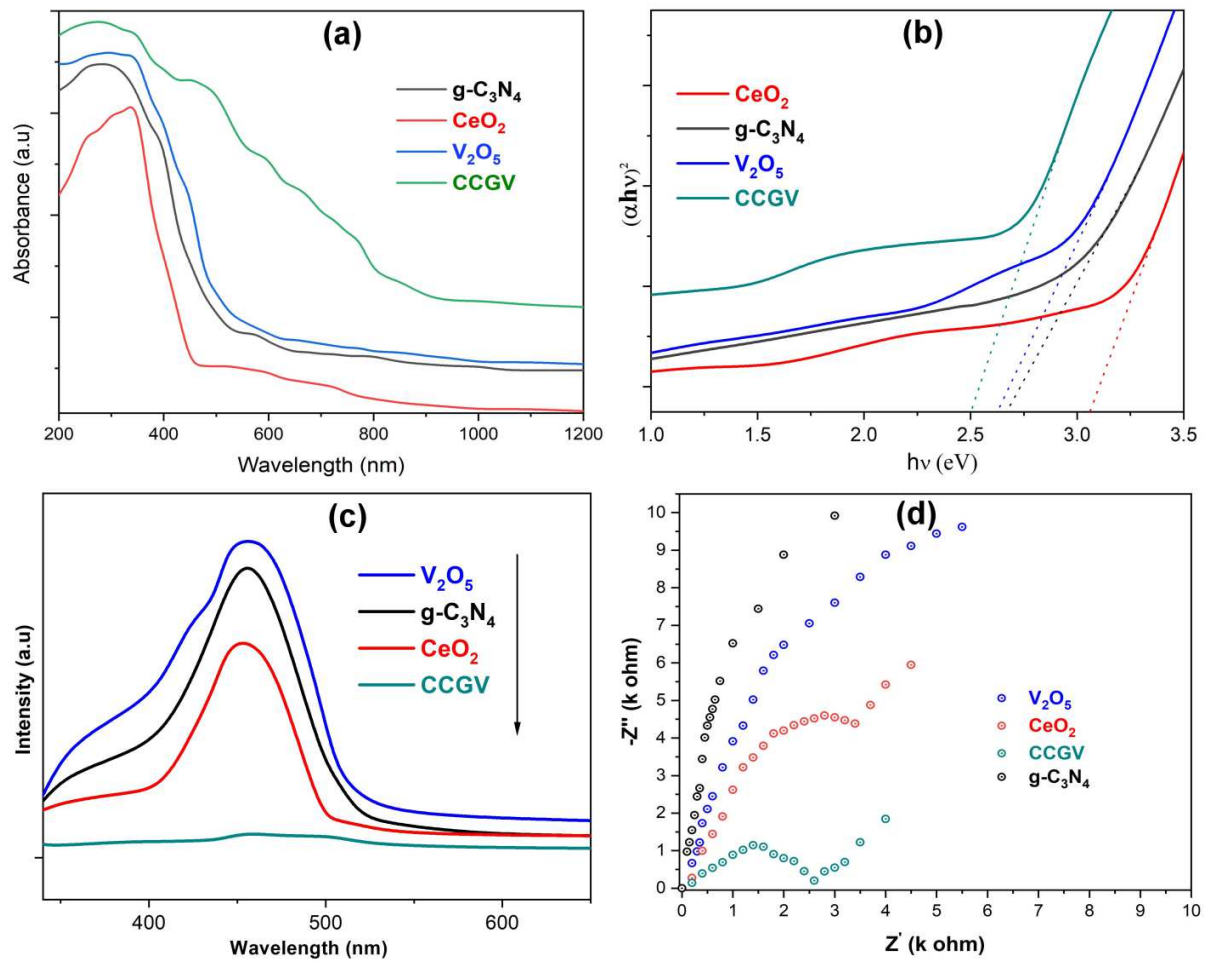


**Figure 5:** (a) UV-DR spectra (b) Tauc plots (c) PL spectra (d) EIS Nyquist plots

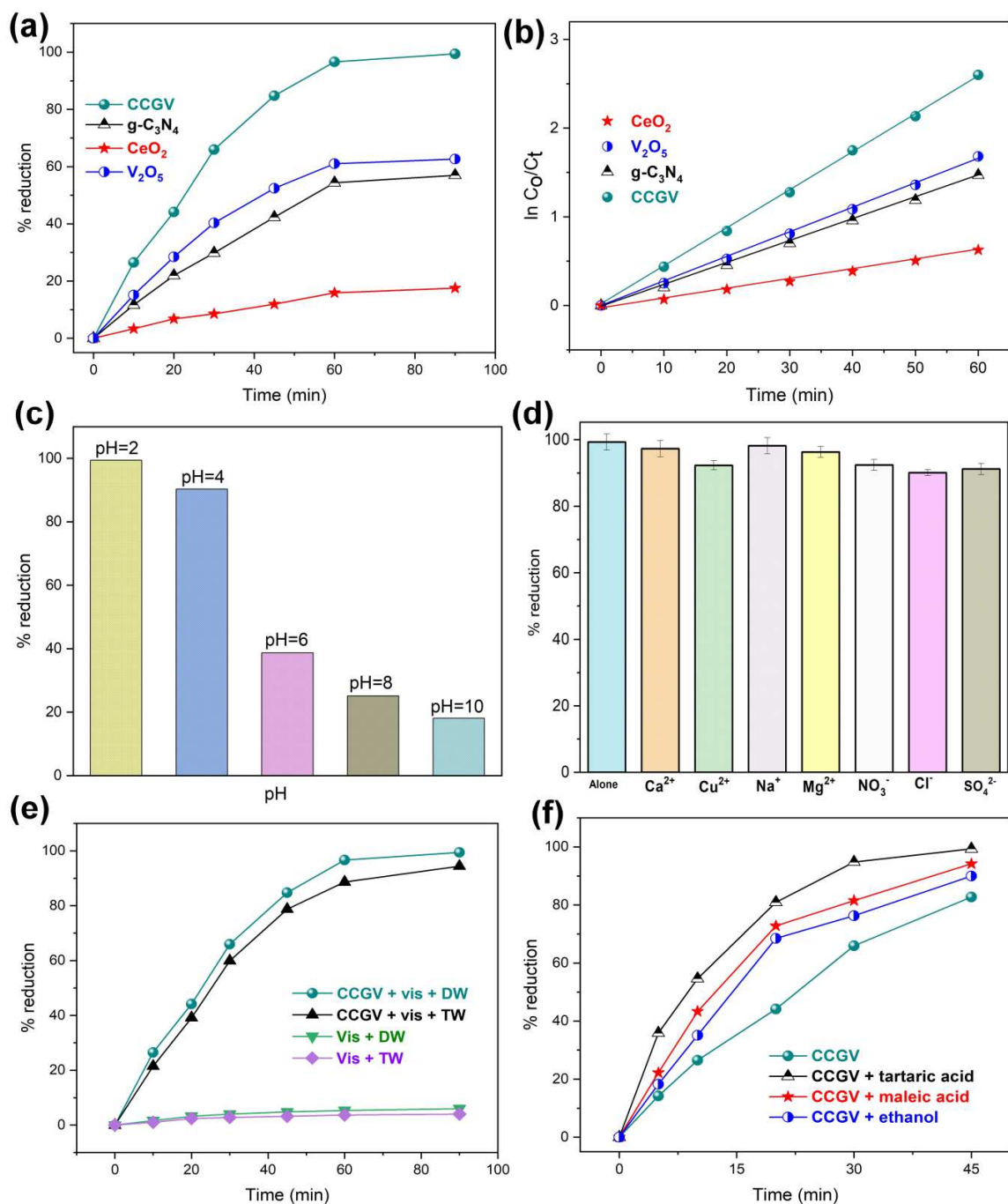


**Figure 6:** (a) The extent of photo-reduction of Cr(VI) under visible light (b) Corresponding kinetics; Effect of reaction parameters onto Cr(VI) photo-reduction with CCGV (c) initial pH (d) electrolytes (e) water matrix (f) Initial co-catalysts or sacrificial agents; [catalyst] = 0.3 mg/mL [Cr<sup>6+</sup>] = 20 mg L<sup>-1</sup>, pH=2, temperature = 30 ± 0.5 °C, Visible light intensity 480 mW cm<sup>-2</sup>

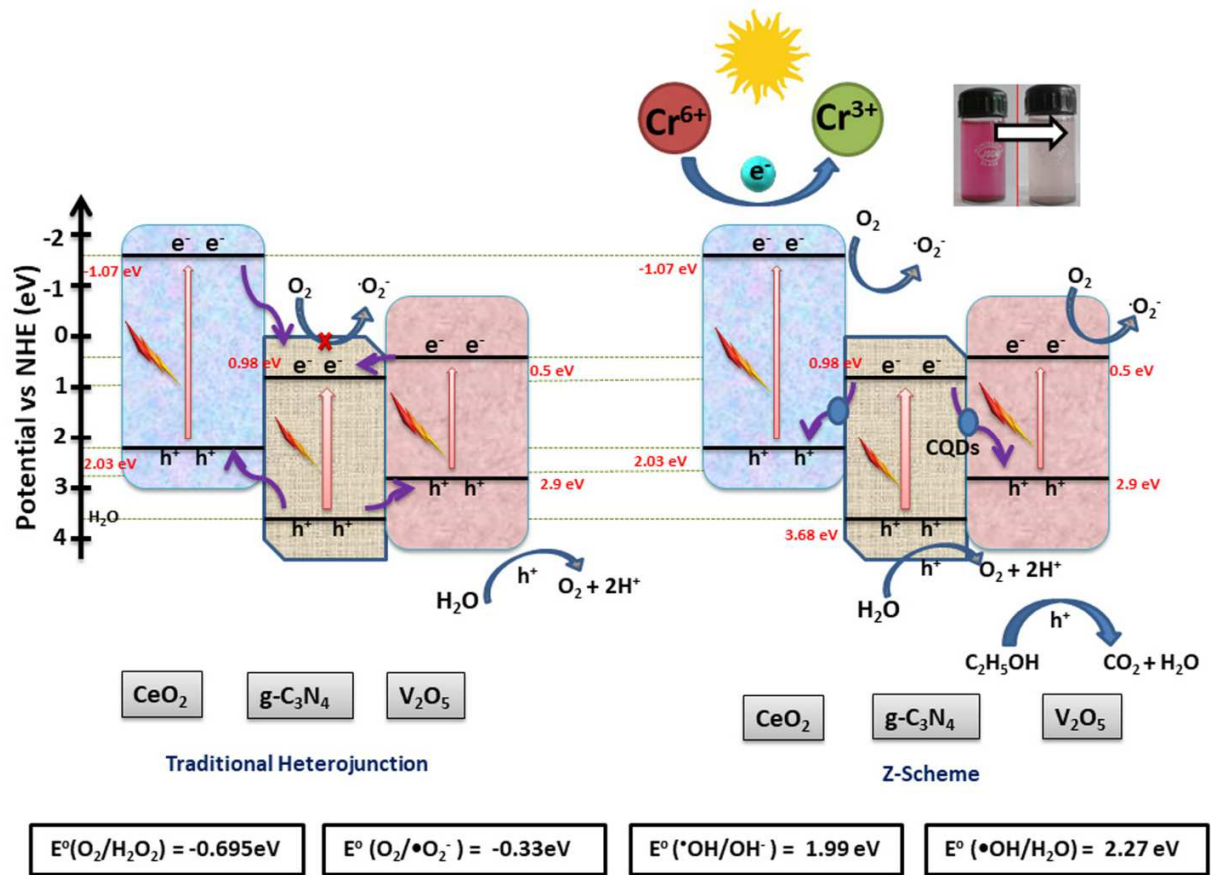


**Figure 7:** Traditional and Z-scheme heterojunction CCGV with possible charge flow

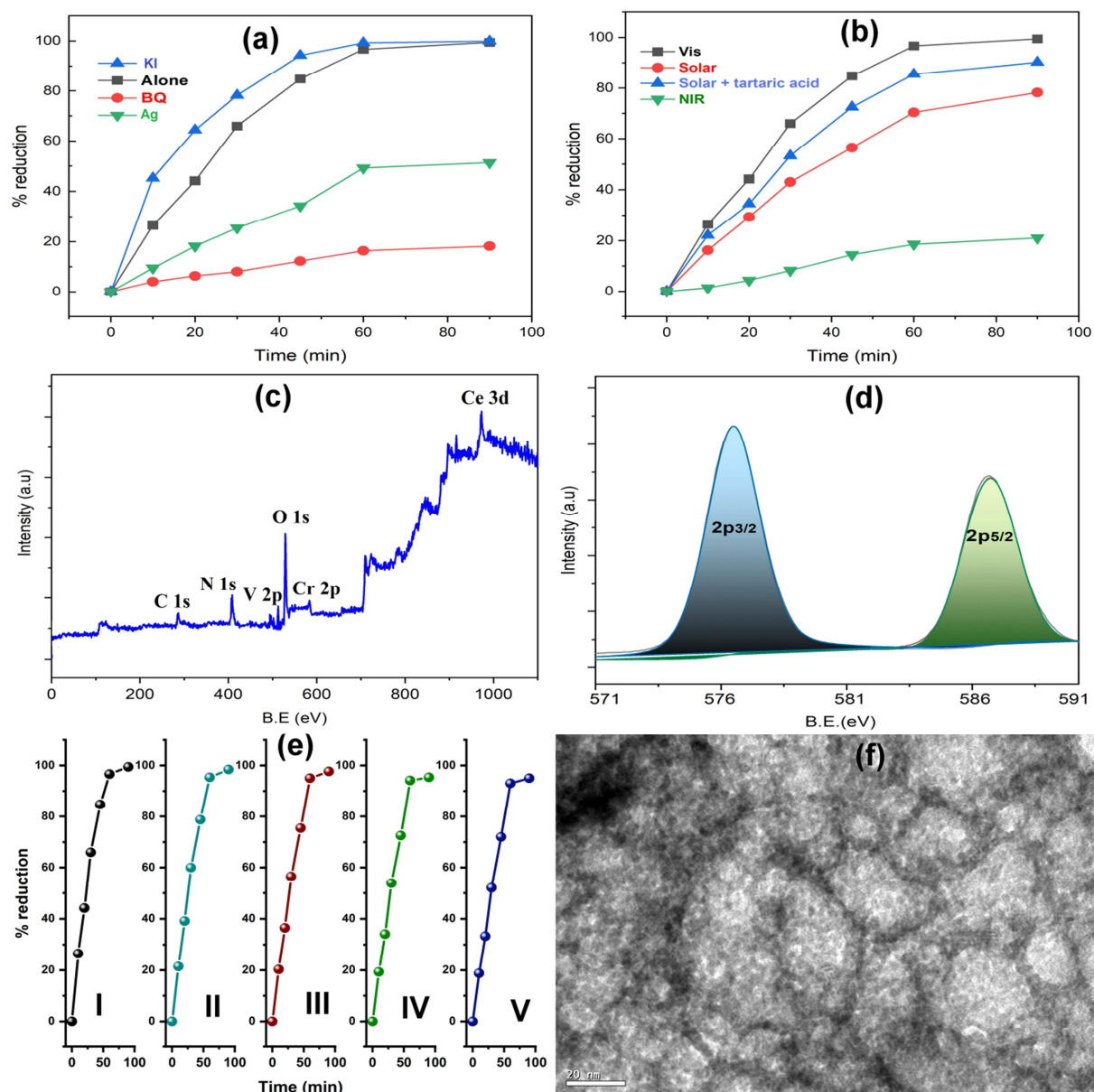
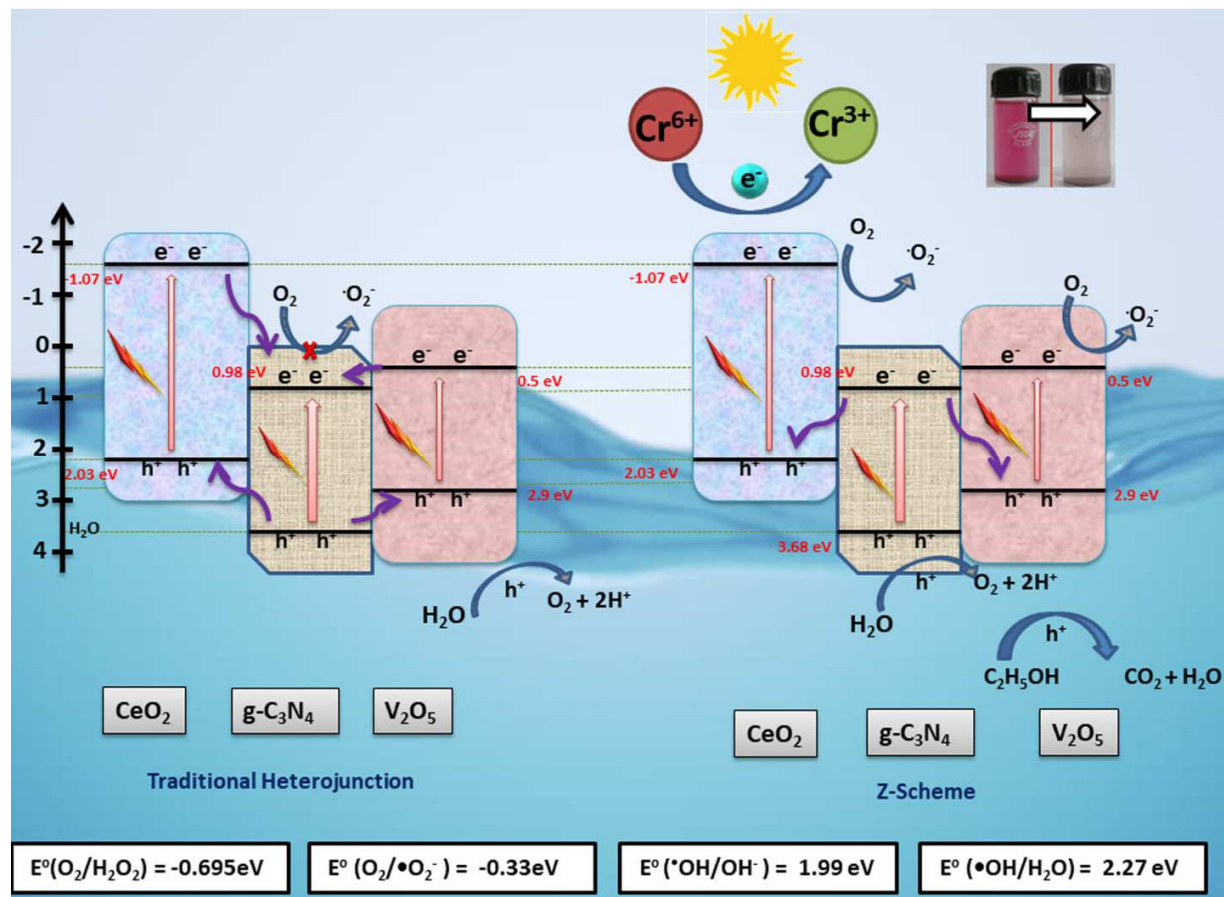


**Figure 8:** (a) Effect of scavengers photo-reduction of Cr(VI) with CCGV under visible light (b) Solar and NIR performance of CCGV (c) XPS survey scan (d) Cr 2p spectrum (Inset) of unused CCGV before final recovery (CCGV + visible + TA system); (e) Reusability studies for Cr(VI) reduction with CCGV under visible light; (f) TEM image of CCGV after use [catalyst] = 0.3 mg/mL [Cr<sup>6+</sup>] = 20 mg L<sup>-1</sup>, pH=2, temperature = 30 ± 0.5 °C, Visible light intensity 480 mW cm<sup>-2</sup>, NIR intensity 200 mW cm<sup>-2</sup>



Graphical abstract

**Highlights**

- Dual Z-scheme CQDs @ CeO<sub>2</sub>/g-C<sub>3</sub>N<sub>4</sub>/V<sub>2</sub>O<sub>5</sub> heterojunction (CCGV) was successfully prepared.
- CCGV junction shows efficient photoreduction of carcinogenic hexavalent chromium
- Visible, NIR and solar activity with high visible capture
- Mechanistic approach-Scavenging and Sacrificial agents
- Comparison between conventional and dual Z-scheme-high potential bands

Journal Pre-proof

**Declaration of interests**

The authors declare that they have no known competing financial interests or personal relationships that could have appeared to influence the work reported in this paper.

The authors declare the following financial interests/personal relationships which may be considered as potential competing interests:

*Amit Kumar*

Dr Amit Kumar  
(Corresponding Author)

Journal Pre-proof